

**A MULTI-SENSOR COMPARISON FOR CORAL REEF HABITAT MAPPING:
A CASE STUDY USING A TROPICAL PATCH REEF ENVIRONMENT IN
BISCAYNE NATIONAL PARK, FLORIDA**

By

DAMARIS TORRES PULLIZA

A thesis submitted in partial fulfillment
of the requirements for the degree of

MASTER OF SCIENCE
in
GEOLOGY

UNIVERSITY OF PUERTO RICO
MAYAGÜEZ CAMPUS
2004

Approved by:

Serge Andréfouët, Ph. D.
Member, Graduate Committee

Date

Wilson Ramírez, Ph. D.
Member, Graduate Committee

Date

Fernando Gilbes, Ph. D.
President, Graduate Committee

Date

Miguel Velez, Ph. D.
Representative, Graduate Studies

Date

Hans Schellekens, Ph. D.
Director, Department of Geology

Date

ABSTRACT

Reef scientists continue exploring methods to better characterize the status of coral reefs environments. In that endeavor, an airborne AISA image (1m, 24 bands) was analyzed together with Ikonos (4m, 3 bands), ASTER (15m, 2 bands), and ETM+ (30m, 4 bands) spaceborne data in order to increase the small number of pilot sites (Turk and Caicos, Tahiti) where multi-sensors comparisons are now available. The benefits of atmospheric and water column correction on the accuracy of image classification maps are also assessed. Water-column correction considered both, the empirical Lyzenga's (1978, 1981) approach and the analytical Maritorena's (1994) model. The latter model requires pixel-specific depth measurements and information on the characteristics of the water column. Bathymetry was collected using an airborne lidar sensor. AISA products were consistently more accurate than spaceborne products with a maximum accuracy of 93%. Also, water column correction proved to be beneficial by generally improving classification accuracy for the processed scenes. Other trends were revealed.

RESUMEN

Investigadores de arrecifes de coral continúan desarrollando métodos que mejoren el modo de evaluar el ambiente coralino. Con similar propósito, se analizó el sensor aéreo AISA (1m, 24 bandas), junto a los sensores espaciales Ikonos (4m, 3 bandas), ASTER (15m, 2 bandas) y ETM+ (30m, 3 bandas) a modo de contribuir al reducido número de estudios (Turk y Caicos, Tahiti) que comparan diferentes sensores con potencial en habientes coralinos. Consideramos además los beneficios provistos mediante la corrección de atmósfera y batimetría a la precisión de mapas béticos. En la corrección batimétrica incluimos el modelo empírico postulado por Lyzenga (1978, 1981) y el modelo analítico de Maritorena (1994). Este último requiere valores de profundidad por pixel y conocimiento general de las propiedades ópticas de la columna de agua. Los datos de profundidad se obtuvieron de medidas colectadas por un sistema aéreo *lidar*. Los mapas temáticos derivados de AISA fueron consistentemente más precisos, con un valor máximo de precisión de 93%, que los obtenidos por sensores satelitales. La clasificación supervisada obtuvo beneficios de la corrección batimétrica. Tendencias adicionales fueron reveladas.

© Copyright by Damaris Torres-Pulliza 2004
All rights reserved

Dedication

This is dedicated to Adriel Isaac, Victoria Catalina and Gabriel Isaac for bringing so much happiness and keeping my spirit up. Also to my family and friends for encouraging and supporting me throughout this long journey.

Acknowledgements

My most sincere thanks go to Serge Andréfouët whose guidance, support and advice throughout this study made it possible and very rewarding. Special thanks go to John Brock at the USGS Coastal and Marine Geology Program for providing the EAARL and AISA data and for the ground truthing fieldwork campaign. I also thank committee members Fernando Gilbes and Wilson Ramirez, and Frank Muller-Karger, Chuanmin Hu, Hernan Santos, Pamela Jansma, Glen Mattioli, Miguel Veléz, and José M. Lopéz for their support. Thanks to the technical and scientific staff at the Institute for Marine Remote Sensing at the University of South Florida for their assistance during this study. The professional and friendly fieldwork team (Dave Palandro from USF; Tonya Clayton and Don Hickey from the USGS) are gratefully acknowledged for their assistance in the field. I thank Richard Curry and staff at Biscayne National Park for use of their facilities. This study was paid in part by the Institute for Marine Remote Sensing - College of Marine Science - University of South Florida, the US Geological Survey, and the Center for Subsurface Sensing and Imaging Systems (CenSSIS).

Table of Contents

List of Tables	ix
List of Figures	x
Appendixes	xi
Chapter 1 – Introduction	1
1.1 Remote Sensing for Coral Reef Mapping	2
1.2 Image Processing	4
1.3 Objectives	5
 Chapter 2 – Methods and Materials	
2.1 Study Area	6
2.2 Data Collection	9
2.2.1 Digital Imagery	10
2.2.1.1 AISA	10
2.2.1.2 IKONOS	11
2.2.1.3 ASTER	13
2.2.1.4 LANDSAT	13
2.2.2 Bathymetric Data	14
2.2.3 Ground Truth Data Collection	14
2.3 Data Processing	15
2.3.1 Pre-Processing	15
2.3.2 EAARL Bathymetric Data	16
2.3.3 Geospatial Positioning	16
2.3.4 Sea Surface Correction	17
2.3.5 Atmospheric Modeling	18
2.3.6 Bathymetric Correction	21
2.3.6.1 Lyzenga’s Model (1978, 1981)	22
2.3.6.2 Maritorena’s <i>et al.</i> Model (1994)	24

2.4 Classification Scheme	26
2.4.1 Geomorphological Structure	26
2.4.2 Benthic Class Definition	27
2.5 Image Classification	28
2.5.1 Data Training	28
2.5.2 Control Data	29
2.5.3 Accuracy Assessment	30
Chapter 3 – Results	
3.1 Performance of Image Correction Methods	32
3.1.1 Atmospheric Correction	32
3.1.2 Bathymetric Correction	32
3.2 Determination of Habitats Classification Scheme	34
3.3 Image Classification Analysis	38
3.3.1 Comparison between Sensors	38
3.3.2 Comparison between Methods	43
3.3.3 Discrimination of Habitat Classes	44
Chapter 4 – Discussion	
4.1 Spectral, Spatial, and Descriptive Resolution	46
4.2 Image Processing and Classification Accuracy	47
4.3 The Reef Environment and Classification Scheme	49
Chapter 5 – Conclusions	58
Reviewed Literature	57

List of Tables

Table 1.	Main characteristics of investigated scenes.	10
Table 2.	AISA visible and NIR spectral bands.	12
Table 3.	Ikonos visible and NIR spectral bands.	12
Table 4.	ASTER visible and NIR spectral bands.	13
Table 5.	Landsat ETM+ visible and NIR spectral bands.	13
Table 6.	Parameters for 6S atmospheric modeling.	19
Table 7.	Modeled coefficient employed to derive above-water remote sensing reflectance.	20
Table 8.	Input parameters for HYDROLIGHT water properties modeling.	25
Table 9.	Interpretation of benthic communities at coarse and fine complexity levels as derived from the Bray-Curtis analysis.	36
Table 10.	Z-test results comparing the significant difference between Tau coefficients for the four sensor images processed to R_{rs} , R_B , and Y_{ij} at seven habitat complexities.	40
Table 11.	Z-test results comparing the significant difference between the classification of AISA, Ikonos, ASTER, and Landsat images processed with three different methods at seven habitat complexities.	44

List of Figures

Figure 1. Map indicating the location of the study area in Biscayne National Park, Florida.	7
Figure 2. Map showing the extent of the study area and general morphology of reef patches.	7
Figure 3. Comparison between synoptic view coverage of studied imagery.	9
Figure 4. The Airborne Imaging Spectro-radiometer (AISA) composite image.	11
Figure 5. Example of an underwater photo-quadrat station.	15
Figure 6. EAARL georectified depth measurements.	17
Figure 7. A comparison between before and after glint removal.	18
Figure 8. Scatter plot of transformed sand spectral values at different depth.	24
Figure 9. Mean spectra of reflectances measured in deep water (R_{∞}).	25
Figure 10. K_d values as estimated by the HYDROLIGHT code.	25
Figure 11. Studied imagery presented using a RGB color composite.	30
Figure 12. Visualization of AISA (top) and Ikonos (below) images before and after water column correction.	33
Figure 13. Visualization of ASTER (top) and Landsat (below) before and after water column correction.	34
Figure 14. Cluster diagram, or dendrogram, showing the similarity of habitat communities among sampled sites.	35
Figure 15. Illustrations representing the different habitat categories used in the classification scheme at a fine complexity resolution.	37
Figure 16. Diagram showing pair of classes consecutive merges following individual SIMPER analysis runs.	38
Figure 17. Comparison of overall accuracy and Tau coefficients for the classification of four sensor images at seven levels of habitat complexities.	41
Figure 18. AISA based image maps derived from a supervised classification of remote sensing bottom albedo values.	42
Figure 19. Image derived thematic maps for nine habitat classes visually showing the relative difficulties for the spaceborne sensors to discriminate spatially small and patchy features.	45

List of Appendixes

- | | |
|--|----|
| Appendix 1. Benthic Sampling Form | 55 |
| Appendix 2. Producer and user accuracies as derived from error matrices for AISA and Ikonos image classification at every habitat complexity and image processing level. | 56 |
| Appendix 3. Producer and user accuracies as derived from error matrices for ASTER and ETM+ image classification at every habitat complexity and image processing level. | 57 |

Chapter 1

1. Introduction

Coral reefs offer a realm of economic and social goods to humans (Moberg and Folke, 1999). In short, they are a source of income, recreation, biodiversity, food, and natural protection against shoreline erosion and storm damage. However, the worldwide coral reef scenery is degrading. Many documents have reported over the past three decades evident signs of deterioration in coral reef communities at local, regional and global scales (Wilkinson, 2002). Those reports do not paint a better panorama for the future of coral reefs, the ecosystem that has been called the rainforest of the oceans (Bellwood & Hughes, 2001). Compiled information suggests that such trend is in part a response to physical and biological natural disturbances. For example, modern corals around the world are experiencing high levels of stress due to what seems to be an ongoing cycle of global climate change similar to those engraved on fossil coral records. Reefs have had the capacity to recover over the perturbations imposed by natural processes in the past. But, more recently, anthropogenic activities are also stressing and quickly degrading such fragile communities to the limits or beyond recovery (Wilkinson, 2002). Increased fresh water run-off, sedimentation, nutrification, oil pollution, overfishing or destructive fishing practices, improper watershed management, ship groundings or people tramping over corals are some of the human related factors that endanger reefs directly or indirectly. Other factors include global greenhouse gases and aerosols emissions, ozone-depleting chemicals usage, and land-use land-cover changes that are all triggering or contributing to global warming and its effects over corals (Kleypas *et al.* 2001). In order to improve our understanding on inherent coral reef processes and effective conservation practices it is important to assess better methods of characterizing the environment and separating the relative influence of natural and anthropogenic stressors at various scales.

1.1 Remote Sensing for Coral Reef Mapping

Thematic maps are of fundamental importance to characterize the marine system. Their enhance interpretability facilitate describing the coral reef physical environment (Andréfouët *et al.* 2002b), identify connectivity to relevant land-based and marine threats (Andréfouët *et al.* 2002a), and to set a baseline reference for change detection analysis (Palandro *et al.* 2003) in a coherent manner. Map production provides the means to display, store, and relate georeferenced spatial data available for analysis and decision-making. Further, the advent of geographic information systems (GIS) made possible to integrate several spatial data sources with more analytic capabilities for interpretation. GIS also facilitates the production of more meaningful maps for environmental modeling and promotes interactive exchange of relevant data between multidisciplinary collaborators. The effective use of those cartographic documents, however, relies on their accuracy reproducing the environment.

Remote sensing technologies offer the synoptic view required to account for the larger land-seascape matrix in the characterization and monitoring of the environment. Traditional methods to gather spatial information became somewhat impractical at that scale, making of remote sensing the most, and in some cases the only, feasible mean to capture referenced data for map production at a suitable spatial resolution (*e.g.* within meters). Throughout the years more sophisticated remote sensing technologies are becoming available. However, the choice of a satellite sensor optimized for the study of coral reef communities seems to still be out of the satellites constellation. These submerged and highly heterogeneous environments impose challenges for benthic habitat mapping and require a specialized sensor. Such challenges not only include dealing with the intervening above water atmospheric path (Gordon, 1992), but also bring the need to account for the contribution of the water surface effects (Fraser *et al.*, 1997; Hochberg *et al.*, 2003b; Mobley, 1999), water column optical attenuating properties (Morel and Maritorena, 2001; Mobley, 1994; Smith and Baker, 1981), and depth variation effects (Lyzenga, 1978, 1981; Maritorena, 1996; Philpot, 1989; Stumpf *et al.*, 2003) to the measured signal. Additionally, the spectral resolution of a sensor designed to better

discriminate reef biological communities require a high number of narrow, properly placed, spectral bands which are not currently available in existing sensors (Hochberg and Atkinson, 2003; Hochberg *et al.*, 2004; Mumby and Edwards, 2002). Optical multi-spectral sensors mounted on aircraft platforms seem to be the more appropriate type to overcome the lack of spectral specialization of satellite sensors. However, the latter lacks the spatial synoptic coverage for large-scale studies and usually cost more.

Three main aspects need to be considered for remote sensing coral reef habitat mapping. Those are spatial resolution, spectral resolution, and the reef system configuration. The relative influence of those three aspects, however, is still unclear (Capolsini *et al.*, 2003; Mumby and Edwards, 2002; Mumby, 2001; Mumby *et al.*, 1998b). To unravel the potentialities of existing sensors in terms of their spatial and spectral resolution, and performance over various environments, few multi-sensor comparisons have been accomplished (Capolsini *et al.* 2003; Andréfouët *et al.* 2002b; Mumby and Edwards 2002; Hochberg and Atkinson, 2003a; Mumby *et al.* 1998b). Those have pointed to some general trends when mapping coral reef habitats. For instance Capolsini *et al.* (2003) and Mumby and Edwards (2002) observations suggest that, if dealing with similar spectral bands but different spatial scales, a higher spatial resolution increase the classification accuracy for fine level habitat mapping. Hochberg, Atkinson and Andréfouët (2003) compared coral reef spectral reflectances collected *in-situ* around the world to those provided by simulated broadband spaceborne sensors, and pointed out the limitations of the latter to spectrally discriminate between sand, coral and algae independently to geographic location. Further, Andréfouët *et al.* (2003a), Capolsini *et al.* (2003), and Mumby *et al.* (1998a) demonstrated the advantages of considering the reef morphology and habitat zonation at reef level (*e.g.* contextual knowledge) to improve image classification accuracy. Additional efforts to validate or unveil trends in terms of thematic map accuracy relative to sensors specification should clarify the relative potentialities of individual sensors for coral reef habitat mapping.

A multi-scale-sensor study should inspect the range of sensors specifications under comparable conditions and same image processing scheme. Otherwise, the relative

comparison may be meaningless. More efforts are needed to account for the different types of reef biota and configurations worldwide by increasing the number of comparative studies and exploring the various image-processing methods and their effects on habitat mapping. To contribute to the small number of pilot sites where multi-sensor comparisons are now available (Turk and Caicos, Tahiti), the relative performance between three broadband multispectral satellite sensors (namely, the medium spatial resolution Advance Spaceborne Thermal Emission and Reflection Radiometer (**ASTER**), and ETM+, and the high spatial resolution Ikonos), and a high-spectral and high-spatial data sensor (*i.e.* the Airborne Imaging Spectroradiometer for Applications (**AISA**)) was evaluated. Other studies have already included Ikonos, Aster and ETM+ sensors. This study is the first presenting the high spatial (1.5 m) and spectral resolution (24 bands between 0.44 and 0.74 nm) AISA sensor for habitat mapping. The case study area, Anniversary Reef, is a small ($\sim 2 \text{ km}^2$) shallow water (2-12 m) patch reef environment which represents quite well the bigger lagoonal patch reef system of Biscayne National Park and the inshore Florida Reef Tract. The suite of sensors under investigation presents a wide range of spatial and spectral resolutions. This allows comparison between the relative influences of sensor's characteristics to the classification accuracy of derived coral reef habitat maps.

1.2 Image Processing

In an effort to generate more accurate maps, different image processing methods are usually applied seeking for better calibration, correction, and enhanced benthic habitat discrimination. A critical step when analyzing radiance values of images collected remotely is to overcome for the absorption and scattering effect of the atmospheric path. This correction becomes more important when attempting a sensor-to-sensor comparison. A relative comparison of scenes collected under different atmospheric conditions, sea-state, viewing geometry, and illumination creates the need of isolating the leaving water reflectance signal from the influence of atmospheric factors.

Another key issue of mapping underwater communities is to compensate for the influence of variable depth on the measured reflectance signal. Water column correction

is expected to improve spectral separability of reef substrates located at different depths and ultimately enhance habitat-mapping accuracy (Mumby *et al.*, 1998a).

The type of selected image classification algorithms may also influence final classification results (Andréfouët *et al.*, 2003b; Capolsini *et al.*, 2003). Identification of the more effective and practical algorithm and methodologies may lead to consensus among reef scientist to follow more homogeneous approaches for coral reef habitat mapping (Green *et al.*, 1996; Mumby *et al.*, 1998a; Andréfouët *et al.*, 2003c).

1.3 Objectives

The main objective of this study is to help reveal the capabilities and limitations of a realm of existing remote sensors for coral reef mapping over a patch reef environment. The influence of different image processing techniques on habitat mapping accuracy is investigated as well. The different options presented to achieve the mapping goes from high-cost (radiative transfer modeling, bathymetric lidar and hyperspectral airborne data) to lower-cost (empirical bathymetric correction, low resolution satellite sensors) approaches.

This thesis is organized in four major sections. The materials and methods chapter illustrate the imagery and specific approaches adopted to collect the ground truth data. It presents the different image processing methods performed for atmospheric and bathymetric correction, including as well ground truth data ordination and habitat classification scheme, image classification, and accuracy assessment approaches. Results and discussion in terms of achieved accuracy of the maps based on extensive ground-truth data and trends are presented on chapter three and four. The most important observations derived from this study and suggestions on the potential of employed imagery and evaluated methods for coral reef habitat mapping are addressed in chapter five.

Chapter 2

2. Materials and Methods

2.1 Study Area

Florida's high latitude reef communities resemble the Caribbean flora and fauna reef environment, only less diverse and with lower vertical relief (Marszalek *et al.*, 1977). Holocene patch reefs, over the Key Largo Limestone formation, are the main features on the gently sloping inner continental shelf. Over 6000 patch reefs exist within the inshore Florida Reef Tract, being more abundant in the upper keys off Key Largo and Elliot Key. These are remnant outcrops of individual massive heads or aggregations of coral heads, providing a topographic relief propitious for coral recruitment (Shinn *et al.*, 1989). Yet, located at the northernmost limit of coral reefs development in the Atlantic, these shelf reef communities are exposed to subtropical marine climate that exerts an important control on reef development and biodiversity (Jaap, 1984). The shallow basin reef system is subjected to thermal stresses, both due to severe winter cold fronts, and high summer temperatures. These variations may quickly alter water temperature and chemistry, potentially resulting in community shifts and lower coral growth. Since the late 70's, Florida reefs have also experienced coral diseases that have rapidly affected reef-builders stony corals and damaged the marine ecosystem (Jaap *et al.*, 2001).

Biscayne National Park (**BNP**), in Florida, is located at the upper end of the Florida Reef Tract and represents a good example of conflicting conservation goal and commercial activities. It is located between the Gulf Stream oceanic current in the East and the sprawling Miami urban area in the North, the Florida Keys ecosystems in the South and the Everglades/Florida Bay wetland/estuaries ecosystems in the West. Biscayne Bay connects this complex seascape of coastal population activities and a sensitive marine environment through natural hydrologic networks, groundwater systems, and currents. Coastal anthropogenic activities have been pointed as a major contributor to the degradation of the coastal marine ecosystem in the Florida Keys. This is explained by an increased flow of nutrient and sediments from land-use practices carried by inland run-off or percolated through the porous limestone bedrock underlying the Keys. Recent

studies have also revealed some connection between humans intestinal bacteria found in coastal waters and diseases killing Florida corals (Porter and Meier, 1992). BNP is a focus center for the study of marine degradation, coral reef research, and establishment of policies for marine resources management.

The case study area encompasses an extension of about 2 km², centered at coordinates 25°23'19" North and 80°09'56" West within BNP (**Figure 1**). This geographic range was selected given the availability of ancillary data relevant to this study and for being representative of the inshore Florida Reef Tract system in the Upper Keys. Abundant reef patches populate the sea floor of this shallow lagoon terrace with depth ranging between 1 to 12 meters and a mean tide range of about 1.18 feet. The study area encloses approximately 200 sand-rimmed patch reefs with the general dome-shape profile that characterize Floridian patches. They exhibit a large range of sizes, varying from 10 to 100 meters in diameter with a vertical relief of 1 to 4 meters at their center axis. The benthic communities associated to these patches are quite heterogeneous and spatially mixed. Its general assemblage consists of abundant octocorals, scattered stony corals, algae, coral rubble, sponges, and seagrass meadows.

Anniversary Reef lies in the center of the area of interest (**Figure 2**), and can be distinguished from the other sub-circular patches by its size and configuration. It exhibits a drop-like shape elongated in its north-south axis (1.5 km) compared to a narrower east-west axis (0.6 km), showing a NNE to SSW trend. Anniversary Reef is a patch platform that rises about 3 meters from the grassy lagoon floor and possesses an irregular topographic relief pattern. The lower areas in the platform are mostly populated with seagrass, sponges, and algae, while the higher topographic features resemble the coral communities of deeper patches with more abundant stony coral cover. Based on the physiographic descriptions presented by Jaap (1984), this reef may be considered a transitional reef that embodies a series of isolated and coalesced patch reefs.

The biotic and geomorphological patchiness of the studied reef system is suitable and challenging to test the potentialities of the spectral and spatial resolution specifications of evaluated sensors for coral reef habitat mapping.

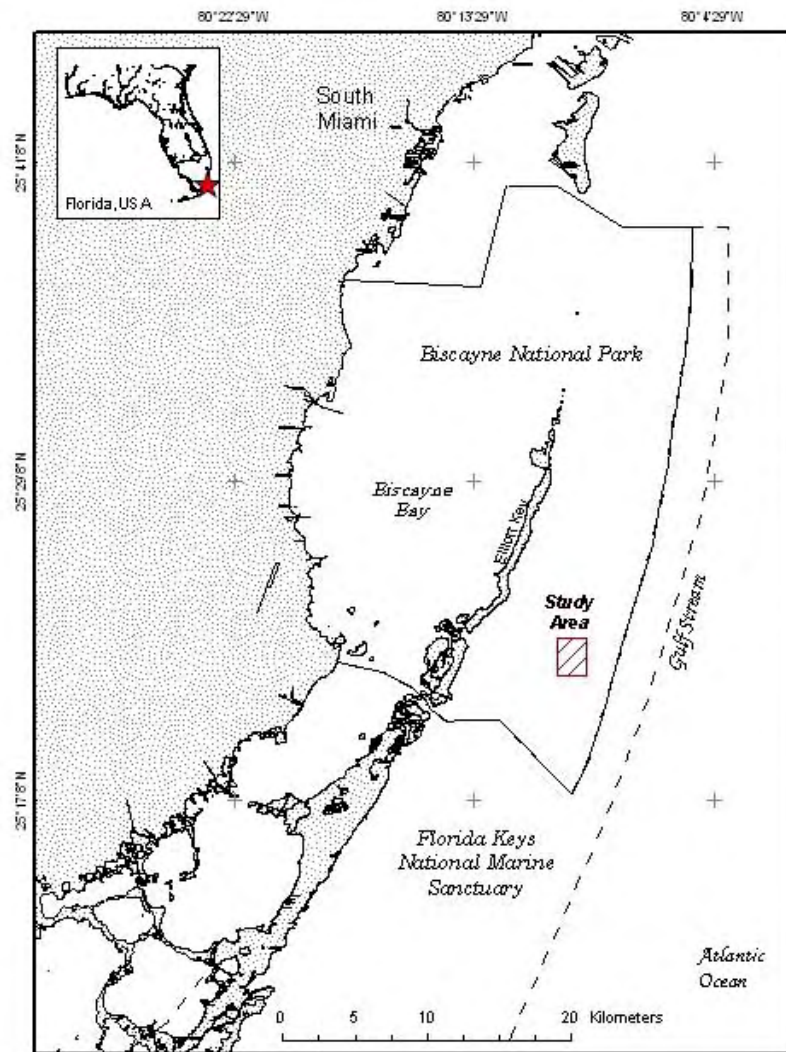


Figure 1. Map indicating the location of the study area in Biscayne National Park, Florida.

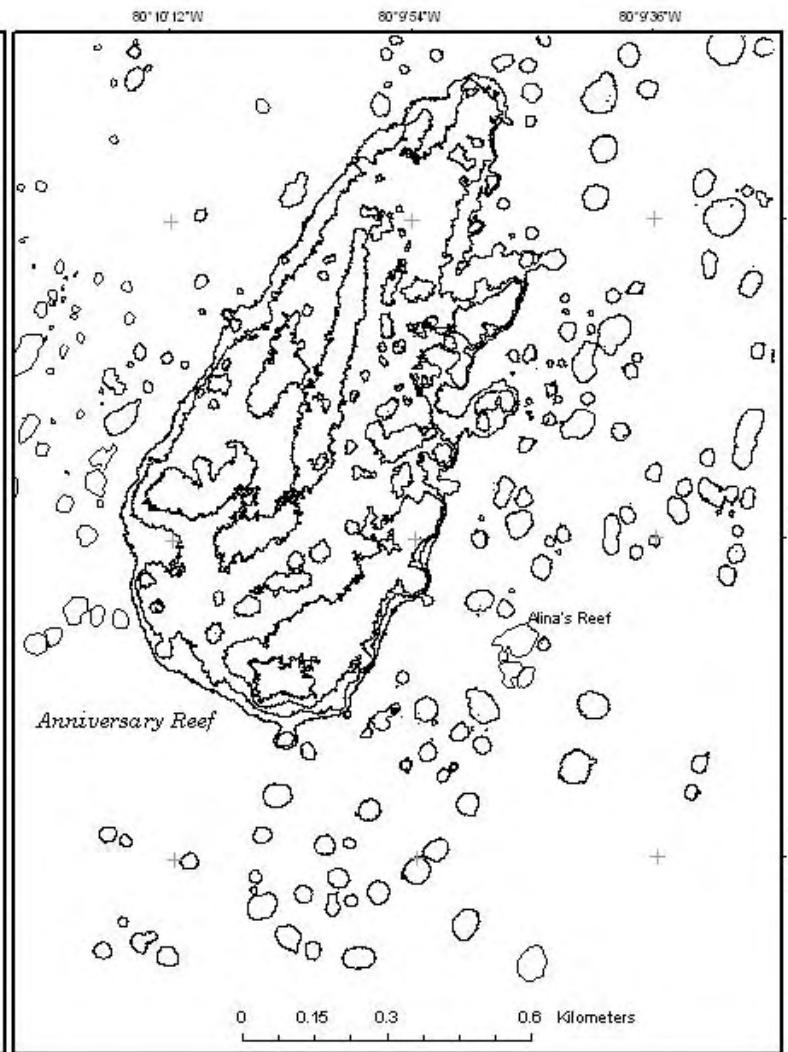


Figure 2. Map showing the extent of the study area and general morphology of reef patches.

2.2 Data Collection

Our database includes AISA, Ikonos, ASTER, and ETM+ imagery together with bathymetric data and ground truth field measurements. The digital dataset was projected to Universal Transverse Mercator (UTM), zone 17, WGS-84 datum, and processed using the Environment for Visualizing Images (ENVI[®] 4) software package. Main characteristics of the images are summarized on Table 1. Imagery was selected for being acquired within one-year time frame of each other and having very low or none cloud cover. This data set represents a suite of modern remote sensors potentially interesting for reef habitat mapping (**Figure 3**). ETM+, for example, provide the area coverage and collection repetition adequate for regional studies and temporal monitoring. However, at a local scale it does not deliver relative high spatial detail. In the other hand, the area coverage and collection repeatability for AISA is highly influenced by the high costs, although it does provides very fine details locally. This analysis uses the visual region of the spectrum since the near infrared (**NIR**) portion is quickly absorbed in the water column making it unsuited for coral reef studies.

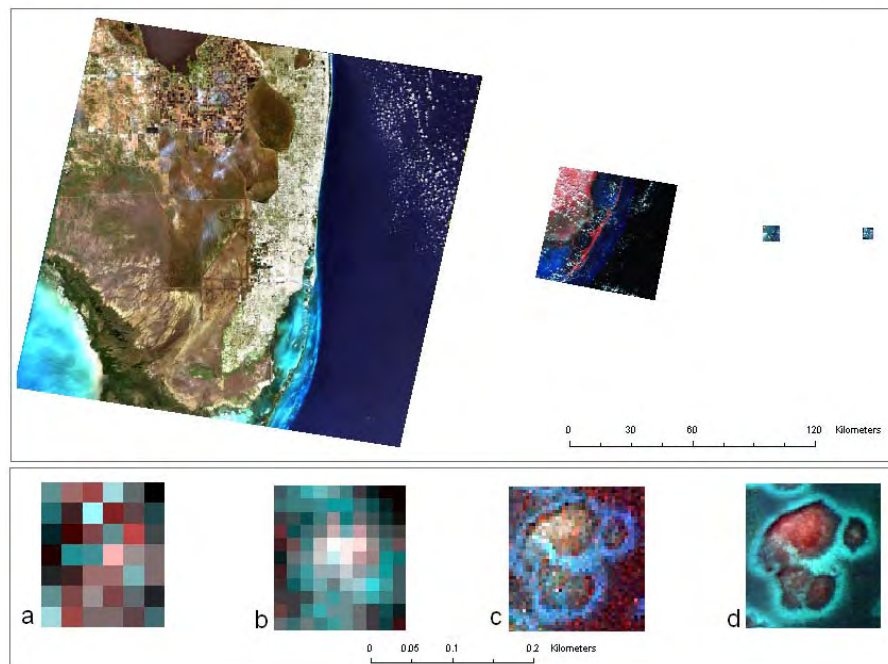


Figure 3. Comparison between synoptic view coverage of studied imagery: ETM+, ASTER, Ikonos, and AISA (a, b, c, d respectively) (top), and spatial resolution contrast between scenes using Alina's Reef as example (bottom).

Table 1. Main characteristics of investigated scenes.

Sensor Specific				
Sensor	AISA	Ikonos	ASTER	ETM+
Platform	Twin Otter	Ikonos-2	EOS TERRA	Landsat 7
Operator	3Di	Space Imaging	NASA/NASDA	NASA
Launch	1997	1999	1998	1999
Sensor altitude (km)	1 to 4	680	705	705
Temporal resolution (day)	On demand	3.5-5	16	16
Number of spectral bands	up to 55	5	15	8
Swath (nadir)	286 pixels	13 km	60 km	185 km
Inclination (deg)	Nadir	Pointable	Sun-sync, 98.2	Sun-sync, 98.2
Image Specific				
Date	7-Jan-2001	18-Mar-2001	25-Sep-2000	5-Feb-2000
Time (GMT)	15:05:00	15:59:00	16:15:11	15:42:34
Digitization (bits/pixel)	16	11	8	8
Spatial resolution (m)	1.5	4	15	30
Relevant spectral bands (VIS)	17	3	2	3
Spectral range (μm)	0.43 - 0.75	0.45 - 0.69	0.52 - 0.69	0.45 - 0.69
Solar azimuth (deg)	~138.79	136.77	150.86	143.68
Solar elevation (deg)	~58.82	34.47	29.66	50.26
Processing level	Orthorectified	Orthorectified	L1B	L1G
Resampling method		NN	CC	NN
Environmental Conditions				
Water vapor (g/cm^2) ¹	2.1	2.3	4.1	1.6
Current wind speed (m/sec) ²	4.2	4.8	3.7	7.3
Total ozone (Dobson units) ³	4.0	260.0	260.0	280.0
Mean Tide Prediction (ft)	0.07	0.37	0.14	1.63
Cloud Cover (%)	0	0 - 5	0 - 14	0 - 9

¹ From Topography Experiment for Ocean Circulation (TOPEX), AISA value from 6S.

² From NOAA FWYF1 station (resides 20 kilometers north of the study area).

³ From Total Ozone Mapping Spectrometer (TOMS), AISA value from 6S.

2.2.1 Digital Imagery

2.2.1.1 AISA

AISA data were acquired by the USGS Center for Coastal and Watershed Studies, Saint Petersburg-Florida, in the morning of January 07, 2001 to assess the capabilities of this hyperspectral sensor for coral reef mapping. The complete AISA data collection comprised an area of 6 km^2 in Biscayne National Park (**Figure 4**). The AISA airborne system, manufactured by Spectral Imaging (Finland), offers high degree of positional

accuracy provided by the combination of Differential Global Positional System (**DGPS**) coupled with an Integrated Navigation System (**INS**) and real time Kalman filter. Concurrent upwelling radiance and downwelling irradiance measurements were acquired and pre-processed by the 3Di Technologies Company. Pre-processing involved radiometric calibration, rectification, and georeferencing attained using calibration files feed to the AISA CaliGeo[®] software. Flight lines were mosaiced at the Institute for Marine Remote Sensing (**IMaRS**), University of South Florida. Operating collection mode of AISA (mode B) allowed user-specified spectral sampling, wavelengths, and number of channels. The 1.5 m ground resolution was achieved by flying at an average nominal altitude of 1500 m. Spectral information of collected AISA data is summarized on **Table 2**. Detailed information for the AISA system can be found at: <http://www.specim.com>.

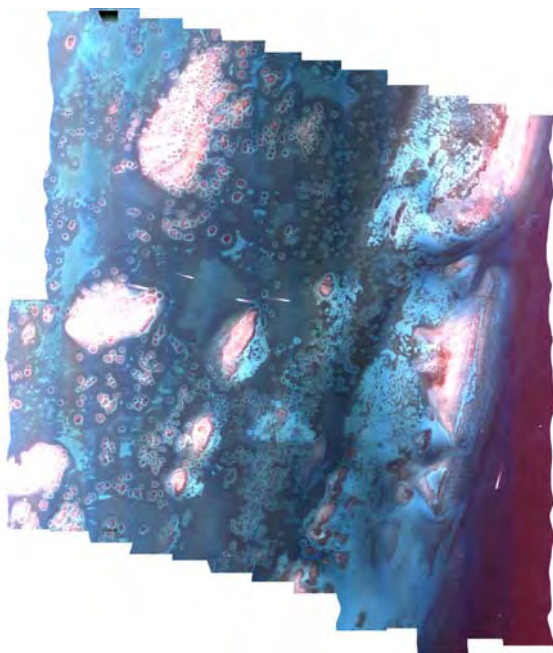


Figure 4. AISA composite image after flight-lines mosaicing and normalization. RGB colors represented with spectral bands 12, 6, and 2 respectively.

2.2.1.2 Ikonos

The Ikonos multiband image was captured in March 18, 2001 and made available by the National Aeronautics and Space Administration (**NASA**) Scientific Data Purchase (**SDP**) program. The 4 m nominal pixel size image is a standard orthorectified product (“Standard Master”). According to NASA specifications, absolute horizontal geodetic accuracy of this product is 12.2 m. Standard Master products are rectified to an earth

ellipsoid using ephemeris data. The Ikonos image in question was radiometrically corrected, has MTFC-off (modulation transfer function compensation-not applied), and was resampled using a Nearest Neighbor algorithm. **Table 3** summarizes Ikonos main spectral characteristics. Refer to the following website for more information: <http://www.spaceimaging.com>.

Table 2. AISA visible and NIR spectral bands

Band No.	Minimum Wavelength	Center Wavelength	Maximum Wavelength	Channel Width	Ground resolution (m)
1	429.43	430.24	431.05	1.62	1.50
2	431.05	435.10	439.15	8.11	1.50
3	442.39	446.45	450.50	8.11	1.50
4	453.74	457.79	461.85	8.11	1.50
5	476.44	480.49	484.54	8.11	1.50
6	487.78	491.83	495.89	8.11	1.50
7	497.51	501.56	505.61	8.11	1.50
8	508.86	512.91	516.96	8.11	1.50
9	518.58	522.63	526.69	8.11	1.50
10	531.55	535.60	539.65	8.11	1.50
11	542.90	546.95	551.00	8.11	1.50
12	554.24	558.30	562.35	8.11	1.50
13	565.59	569.64	573.69	8.11	1.50
14	575.15	579.48	583.81	8.66	1.50
15	587.28	591.61	595.94	8.66	1.50
16	599.40	603.73	608.06	8.66	1.50
17	611.53	615.86	620.19	8.66	1.50
18	621.92	626.25	630.58	8.66	1.50
19	632.31	636.64	640.97	8.66	1.50
20	644.43	648.76	653.09	8.66	1.50
21	656.56	660.89	665.22	8.66	1.50
22	666.95	671.28	675.61	8.66	1.50
23	677.34	681.67	686.00	8.66	1.50
24	689.47	693.80	698.13	8.66	1.50
25	718.91	723.24	727.57	8.66	1.50
26	743.16	747.49	751.82	8.66	1.50

Table 3. Ikonos visible and NIR spectral bands

Band No.	Minimum Wavelength	Center Wavelength	Maximum Wavelength	Channel Width	Ground resolution (m)
1	444.70	480.30	516.00	71.30	4
2	506.40	550.70	595.00	88.60	4
3	631.90	664.80	697.70	65.80	4
4	757.30	805.00	852.70	95.40	4
Pan	525.80	727.10	928.50	403.00	1

2.2.1.3 ASTER

The ASTER image was acquired in September 25, 2000. It is a Level 1B (L1B) data product supplied by the USGS Eros Data Center Distributed Active Archive Center (USGS-EDC-DAAC). The image is radiometrically calibrated and geometrically corrected. The Cubic Convolution (CC) algorithm was used for resampling. The visible range of the ASTER image (0.52 to 0.69 μm) is confined within two broad spectral bands (band no. 1 and 2) having a spatial resolution of 15 m (**Table 4**). More information is available at the ASTER User Handbook (<http://asterweb.jpl.nasa.gov>).

Table 4. ASTER visible and NIR spectral bands

Band No.	Minimum Wavelength	Center Wavelength	Maximum Wavelength	Channel Width	Ground resolution (m)
1	520	560	600	80	15
2	630	660	690	60	15
3N	780	820	860	80	15
3B	780	820	860	80	15

2.2.1.4 ETM+

The Landsat ETM+ image was gathered in February 5, 2000 and was provided by the USGS-EDC-DAAC as a level 1G (L1G) product. An L1G image has undergone radiometric and geometric corrections. The used image was generated by the Level 1 Product Generation System (**LPGS**), was resampled using the Nearest Neighbor method, and is located on the path/row 015/042 within the World Reference System. **Table 5** summarizes ETM+ spectral configuration. For more specific information on the Landsat 7 program, ETM+ sensor, and data products refer to:

http://ltpwww.gsfc.nasa.gov/IAS/handbook/handbook_toc.html.

Table 5. ETM+ visible and NIR spectral bands

Band No.	Minimum Wavelength	Center Wavelength	Maximum Wavelength	Channel Width	Ground Resolution (m)
1	450	485	520	70	30
2	530	570	610	80	30
3	630	655	660	60	30
4	780	840	900	120	30
Pan	520	710	900	380	15

2.2.2 Bathymetric Data

During the summer of 2001 the NASA Experimental Advanced Airborne Research Lidar (**EAARL**) was flown over the Florida Keys Reef Tract as part of a mission to test the performance of this Light Detection and Ranging (**lidar**) system over a shallow water reef environment (Brock *et al.*, 2004). EAARL makes use of a precision GPS network to monitor the aircraft attitude, and to establish an accurate 3D geolocation above the WGS-84 ellipsoid. An average pulse repetition frequency of 3000 Hertz allows closely spaced measurements to depict subtle subaerial and seafloor topographic changes. It uses electromagnetic radiation, in a narrow beam attenuation mode, to measure signal return time. Such measurements are adjusted to the light-transmission properties of the air and water to determine water depth and above water altitudes. Details on EAARL are provided in Wright and Brock (2002). EAARL data were utilized to generate a digital elevation model of the seafloor in the study area.

2.2.3 Ground Truth Datasets

The field campaign was designed to collect ground truth data optimized to the 1.5 m spatial resolution of AISA. *A priori* knowledge of the area together with unsupervised classification (*i.e.* ISODATA) was the criteria used to classify the AISA image into four coarse benthic classes. The resulting preliminary map provided the leading strata to generate the random points to be used in a stratified sampling approach (Congalton, 1991). A number of 30 random points per strata were generated using an automated computer based technique. A benthic habitat sampling data sheet, to be filled at each field station, was designed to guide the assessment and to maintain consistency between surveyor observations (**Appendix 1**).

The field campaign was carried out on March 2002. Benthic communities were described following the photo-quadrat technique using a 1m² submersible quadrat (**Figure 5**). Additionally, a short (1 minute) underwater video of the neighboring area was acquired at every station. Video recording was utilized for further visual reference and to allow extrapolation of station observations to the coarser resolution images. Benthic communities were characterized and visually quantified based on percent cover

within each 1m² quadrat. Hard coral taxon was described at a genus level except where continuous stony coral covered an area bigger than the quadrat perimeter. In such cases, those were recorded to species level. Observers were towed between stations as a way to manage the time more efficiently and to detect any remarkable feature on the way to consecutive stations (*e.g.* three big (~4 m) massive *Montastraea annularis* heads were identified and georeferenced). Every station was georeferenced using a Precision Lightweight GPS Receiver (PLGR+96 – PPS) with a positional uncertainty of ± 3 meters. A total of 102 stations were surveyed during the field campaign. Eighteen of the proposed field stations were not accomplished due to time and weather constrains. Additionally to the visited stations, two 100 m long video-transects were surveyed over Anniversary Reef to represent gradational transitions between benthic communities.



Figure 5. Example of an underwater photo-quadrat station, showing the 1m² scaled quadrat, station ID slate to keep record of photography, and BNP typical biota.

2.3 Data Processing

2.3.1 Pre-processing

Digital numbers were converted to physical units of calibrated radiance ($\text{W m}^{-2}\text{sr}^{-1}\text{nm}^{-1}$) using the equations and calibration coefficients provided by the sensor technical handbooks and online official information.

2.3.2 EAARL Bathymetric Data

Some suspicious depth values were identified on the EAARL dataset. Those were more likely due to water turbidity. Indeed, water properties places limitations on whether lidar optical measurements represent actual depth. Most of the noise was seen at depth greater than 6 meters and mainly over the seagrass beds.

In order to discard erroneous values, the georeferenced depth measurements (*i.e.* x, y, z) were examined by creating region statistics within a size-controlled window. Depth values that deviated significantly from the window mean depth were evaluated. The AISA image was subsequently inspected to avoid eradication of true ground features (*e.g.* small patch reefs). Suspicious depth spikes were filtered out to restore the expected smoother appearance of the fairly flat seagrass beds. Once filtering was accomplished the corrected data set was gridded using the kriging interpolation method incorporated in the ArcMap 8.2 software (**Figure 6**). Four different DEM were generated from the point dataset to correspond with the pixel size of the four studied images (*i.e.* 1.5, 4, 15, 30 meters respectively).

2.3.3 Geospatial Positioning

The data set was rectified to the AISA coordinate system so that field data ground positioning could be better constrained and to maintain geographic integrity for all data. With AISA as master, the satellite images were georectified when necessary applying the Nearest Neighbor resampling approach. The Nearest Neighbor algorithm was selected to avoid averaging pixel information with surrounding values.

To assure appropriate positioning of depth information, remarkable features were identified within the bathymetric data. Isolated coral heads, escarpments, or any other identifiable feature that could be related to elements observed in AISA, were used as ground control points. Isobaths were generated from rectified DEMs and overlapped over the imagery for quality control.

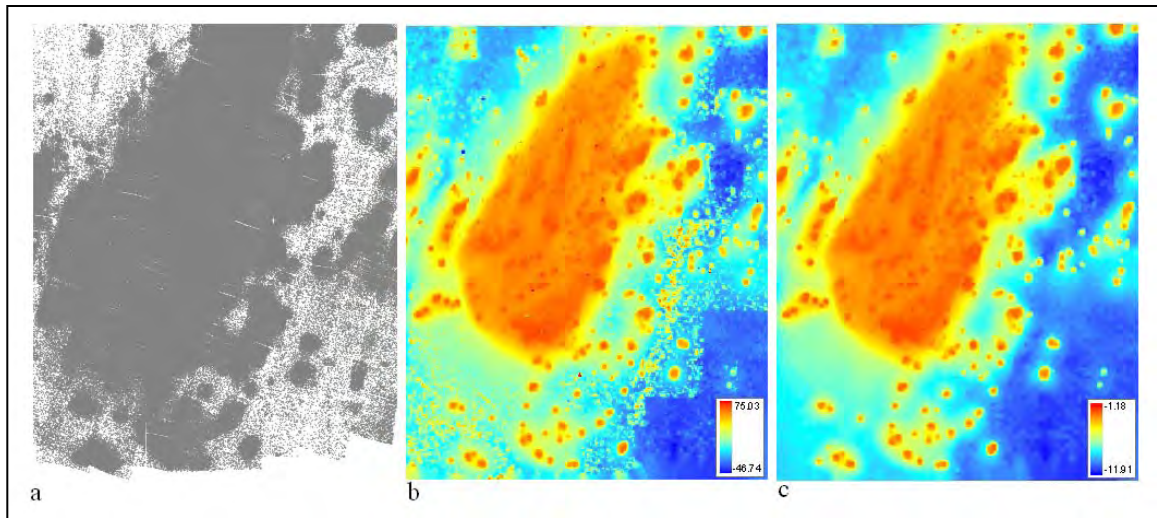


Figure 6. (a) EAARL georectified depth measurements. (b) DEM obtained from the interpolation of unfiltered depth data points. (c) DEM generated from the interpolation of filtered depth data points.

2.3.4 Sea Surface Correction

Visual inspection of the Ikonos image revealed the influence of wind-driven waves and resulting sunglint at the sea surface. Such effect obstructs visual recognition of subsurface features and may bias image statistics on a benthic habitat classification approach. Wave-induced specular reflectance effects (*i.e.* glint) were removed by applying the method presented on Hochberg *et al.* (2003b) (**Figure 7**). This method assumes that the near-infrared region (**NIR**) of the spectrum (*i.e.* band 4 in Ikonos) is totally absorbed by the water. Thus, any recorded NIR upward radiance above a water body should contain the reflected sunlight, as a function of geometry. Assuming that the glint effect remains relatively constant independently of wavelength then the NIR can be used to lead the recognition and removal of sunglint across wavelengths in the visible (**VIS**) range. The glint correction was performed after correcting for the atmospheric effect. For a more complete understanding of the method and algorithm refer to Hochberg *et al.*, 2003.

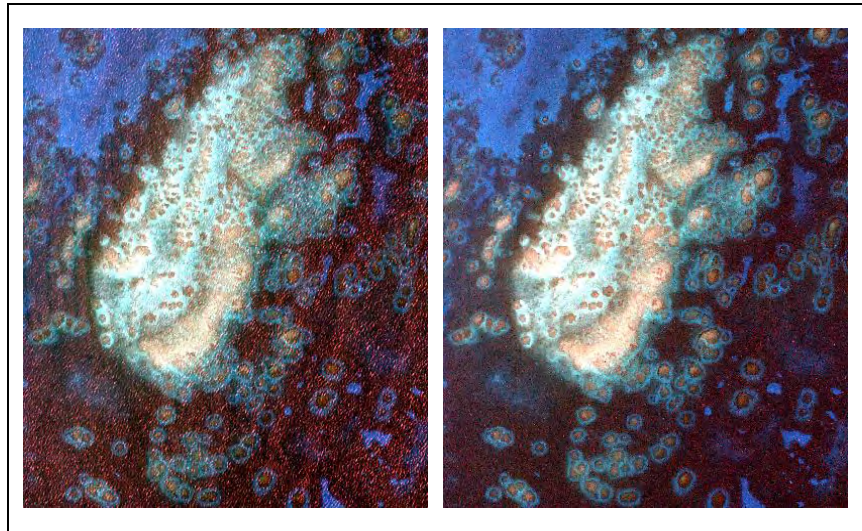


Figure 7. Ikonos images showing before (left) and after (right) glint removal results over the study area.

2.3.5 Atmospheric Modeling

This study used different models to estimate the contribution of the atmosphere to the at-sensor measured signal. No ancillary data or atmospheric measurements were available to describe scene-specific optical conditions of the atmosphere at sensor overpass. Thus, parameters were modeled using the radiative transfer numerical models 6S version 2.0 (Vermote *et al.*, 1997) and Hydrolight 4.1 (Mobley *et al.*, 1995). Informational gaps to describe atmospheric constituents (*i.e.* ozone, water vapor) or air-water surface conditions (*i.e.* wind speed) were filled with historical archived data (**Table 1**). Every computed parameter is considered λ (wavelength) dependent, but this term was omitted for brevity.

Radiation undergoes significant attenuation in its double journey through the atmosphere (*i.e.* sun-target-sensor). The two critical processes are the absorption due to atmospheric gases, and scattering due to atmospheric aerosols and molecules content. The scattering factors, $L_{rayleigh}$ and $L_{aerosol}$, refers to molecular and aerosol scattering respectively. The latter also considers multiple scattering between the two types. The spectral radiance (L) that does not reach the target but that is scattered upward to the sensor is known as atmospheric path radiance (L_{atm}) and is expressed as:

$$L_{atm} = L_{rayleigh} + L_{aerosol} \quad (1)$$

Total radiance (L_{total}), as seen by a remote sensor, is the sum of the spectral radiances arriving from the atmosphere (L_{atm}), plus the target radiance (L_{target}) after being transmitted from the target to the sensor through the atmosphere (Hu and Carder, 2002):

$$L_{total} = L_{atm} + t L_{target} \quad (2)$$

where t is the diffuse transmittance for propagation. The 6S code was employed to model t and to derive L_{atm} . Parameters used in the different runs are shown in **Table 6**, and the coefficient values are as in **Table 7**. Atmospheric corrections provide the signal just above the water surface.

Table 6. Parameters for 6S atmospheric modeling

Parameters	Values
Atmospheric Model	Tropical
Aerosol Model	Maritime
Visibility	35 km
Target Altitude	at sea level
Sensor Altitude	Refer to Table 1
Environmental Conditions	Refer to Table 1
Ground Reflectance Type	Homogeneous surface
Ground Reflectance Target	Mean spectral value of clear water

Over water, as opposed to atmospheric correction for land applications, is necessary to also consider the optical properties of the sea surface including the reflected skylight and the solar glitter reflection (Mobley, 1999). The combination of such effects together with the inherent light absorbing and scattering properties of the water column reduces the radiance signal of the target (*i.e.* water-leaving radiance, L_w) to a 10 – 15 % when registered at the satellite sensor (Hu and Carder, 2002). Water column corrections methods are discussed in the next section.

Table 7. Modeled coefficient employed to derive above-water remote sensing reflectance

AISA								
Wavelength nm	t	E_d W/m ² *nm	ρ	L_{atm} W/m ² *sr*nm	F_0 W/m ² *nm	L_{sky} W/m ² *sr*nm	R_∞ sr ⁻¹	K_d m ⁻¹
430	0.9747	0.5463	0.0246	0.0046	1.1380	0.0005	0.0062	0.0594
435	0.9753	0.6466	0.0238	0.0068	1.7270	0.0006	0.0058	0.0605
446	0.9767	0.7561	0.0223	0.0070	1.8960	0.0006	0.0054	0.0608
458	0.9782	0.8016	0.0207	0.0067	1.9760	0.0006	0.0051	0.0598
480	0.9801	0.8264	0.0184	0.0062	2.0400	0.0006	0.0047	0.0570
492	0.9817	0.7995	0.0173	0.0054	1.9010	0.0006	0.0042	0.0581
502	0.9825	0.8011	0.0165	0.0051	1.8990	0.0005	0.0037	0.0629
513	0.9834	0.7869	0.0155	0.0048	1.8660	0.0005	0.0028	0.0765
523	0.9839	0.7906	0.0148	0.0046	1.8990	0.0005	0.0025	0.0817
536	0.9846	0.8130	0.0139	0.0043	1.8760	0.0005	0.0023	0.0838
547	0.9851	0.8186	0.0133	0.0040	1.8380	0.0005	0.0020	0.0915
558	0.9857	0.8079	0.0127	0.0037	1.7920	0.0005	0.0017	0.0981
570	0.9861	0.8090	0.0121	0.0035	1.7740	0.0004	0.0015	0.1080
579	0.9865	0.8208	0.0117	0.0035	1.8330	0.0004	0.0012	0.1330
592	0.9869	0.7474	0.0112	0.0033	1.8130	0.0004	0.0007	0.2120
604	0.9874	0.7843	0.0107	0.0031	1.7810	0.0004	0.0004	0.3290
616	0.9878	0.7780	0.0103	0.0027	1.6130	0.0004	0.0004	0.3720
626	0.9882	0.7571	0.0099	0.0028	1.7010	0.0004	0.0003	0.3920
637	0.9885	0.7523	0.0096	0.0026	1.6580	0.0004	0.0003	0.4240
649	0.9888	0.7177	0.0093	0.0024	1.5620	0.0003	0.0003	0.4620
661	0.9890	0.6942	0.0090	0.0023	1.5750	0.0003	0.0002	0.5650
671	0.9893	0.7051	0.0087	0.0022	1.5200	0.0003	0.0002	0.6080
682	0.9895	0.6790	0.0085	0.0021	1.4830	0.0003	0.0002	0.6450
694	0.9897	0.5949	0.0082	0.0020	1.4400	0.0003	0.0001	0.7480
							$\theta_0 = 58.82$	1/7/01 15:05
IKONOS								
480	0.8966	1.3823	0.0728	0.0375	1.9461	0.0015	0.0048	0.0475
550	0.9329	1.3281	0.0454	0.0223	1.8575	0.0012	0.0019	0.0789
664	0.9596	1.1271	0.0254	0.0105	1.5580	0.0009	0.0002	0.4850
							$\theta_0 = 33.84$	3/18/01 15:59
ASTER								
660	0.949	1.200	0.026	0.011	1.543	0.001	0.0018	0.000
810	0.964	0.909	0.016	0.005	1.121	0.001	0.0002	2.580
							$\theta_0 = 29.75$	9/25/00 16:15
Landsat 7 ETM +								
482	0.8974	1.0253	0.0789	0.0317	1.9690	0.0017	0.0047	0.0047
565	0.9369	0.9779	0.0459	0.0173	1.8429	0.0013	0.0016	0.0016
660	0.9589	0.8625	0.0281	0.0109	1.9014	0.0011	0.0002	0.0002
							$\theta_0 = 50.17$	2/5/00 15:43

Solving equation 2 for water-leaving radiance (L_w) just above the sea surface and accounting for the reflected skylight (L_{sky}) we have:

$$t L_{target} = t L_w + L_{sky} \quad (3)$$

thus;

$$L_w = \frac{(L_{total} - L_{sky} - L_{atm})}{t} \quad (4)$$

Water-leaving radiance is then normalized by the incident downwelling irradiance (E_d) to yield remote sensing reflectance:

$$R_{rs} = \frac{L_w}{E_d}$$

The latter is a measure of how much incident downwelling light makes its way back up to the sensor from the water surface (Mobley, 1999; Toole *et al.*, 2000). The reflected skylight and downwelling irradiance factors for clear-sky conditions were estimated using the Gregg and Carder (1990) RADTRAN model implemented in the Hydrolight 4.1 code (Table 7). Considering that the study area is relatively small, homogeneous atmospheric conditions within each individual image were assumed.

2.3.6 Bathymetric Correction

The process of remote sensing coral reef habitat mapping consists in assigning bottom reflectances to benthic classes. As the atmosphere, the water medium interacts with the radiant flux and modifies it in such a way that the spectral characteristics of a substrate type at various depths can be confused with that of a totally different substrate (*e.g.* shallow seagrass confused with deep sand). Variations in water-depth tend to attenuate habitat spectral contrast, which influences then statistical based image classification. To obtain a depth-independent spectral measurement of the substrate is necessary to compensate for the water column effect (Mumby *et al.*, 1998a).

Solar radiation entering a water body attenuates in an exponential manner with increasing depth (Gordon, 1992). The severity of the light exponential decay is dependant on the absorbing properties of the water medium and measured wavelength. A number of models have been developed that can be used to compensate for the effect due to the water column. Most of them require water optical measurements and pixel-based depth information (Gordon and Brown 1974; Philpot, 1989; Mobley *et al.*, 1993; Lee *et al.*, 1994; Maritorena *et al.*, 1994; Maritorena, 1996; Lee *et al.*, 1999). Others account for the water column effect using empirical approaches (Lyzenga 1978, 1981). Two of these approaches were chose, the analytical technique presented by Maritorena *et al.* (1994) and the empirical image-based approach by Lyzenga (1981). These were selected to compare their relative benefits on image classification accuracy, considering as well data processing timing and data requirements.

2.3.6.1 Lyzenga's Model (1978, 1981)

This approach takes the most of the spectral information without the requirement of having ancillary data. Instead of deriving substrate spectra accounting for the depth and water properties, this method transforms spectral values into a 'depth-invariant index of the bottom types'. If the logarithm of reflectances of a pair of bands is plotted against each other the spectral values for a constant bottom type at variable depths should follow a straight line (Lyzenga *et al.*, 1978). Different bottom types should provide different parallel lines. The main limitation of this approach, among others, is that it needs to be employed over clear waters (*i.e.* Jerlov water Type I or II). However, our study area fulfills such requirement.

A number of pixels representing the same bottom type are selected (*i.e.* sand). Since the study area does not include large areas of the same substratum at different depths it was necessary to collect sand pixels outside of it. Sand pixel regions were chosen by ground truth and visual observations. Lyzenga's algorithm was applied to the atmospherically corrected scenes (*i.e.* R_{rs} values).

The model assumes that the bottom-reflected radiance is approximately a linear function of the bottom reflectance and an exponential function of the water depth (Lyzenga, 1981). The first step is to relate the exponential decay of sand reflectance due to increasing depth. Sand reflectance values are linearised using [6]:

$$X_i = \ln(\rho_i) \quad (6)$$

where ρ_i is the atmospherically corrected reflectance (R_{rs}) for band i . The scatter bi-plot of transformed values for bands (X) i and j of a relatively uniform bottom type should reveal a linear trend as on **Figure 8**. Second, the slope of the correlation between the selected pair of bands (ij) provides the attenuation coefficient ratio (k_i/k_j) with:

$$\frac{k_i}{k_j} = a + \sqrt{a^2 + 1} \quad (7)$$

where

$$a = \frac{\sigma_{ii} - \sigma_{jj}}{2\sigma_{ij}} \quad (8)$$

and

$$\sigma_{ij} = \overline{X_i X_j} - \overline{X_i} \overline{X_j} \quad (9)$$

(i.e. σ_{ii} and σ_{jj} are the variances for i and j measurements respectively, and σ_{ij} is the covariance between i and j). Having derived k_i/k_j the final step is to calculate the bottom-type index (Y_{ij}) by:

$$Y_{ij} = \ln(\rho_i) - \left[\left(\frac{k_i}{k_j} \right) \ln(\rho_j) \right] \quad (10)$$

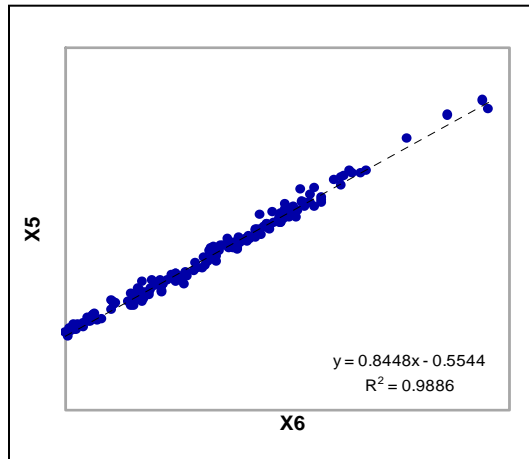


Figure 8. Scatter plot of transformed sand spectral values at different depth showing AISA bands (X) 5 and 6.

2.3.6.2 Maritorena's *et al.* Model (1994)

This analytical model seeks to relate above water remote sensing reflectance (R_{rs}) to bottom remote sensing reflectance (R_B). The formula involves the effective attenuation of the water column, reflectance of optically deep water, and water column thickness. First, it assumes that the upwelling irradiance just below the surface can be decoupled into the flux backscattered by the water column and the bottom reflectance (R_B). Thus, it is necessary to estimate and subtract the influence of the water column flux, accounting for its optical properties, to approximate the bottom reflectance.

If the attenuation of a water column limited by a black bottom and the reflected flux immediately above the bottom, where the bottom is a Lambertian reflector, occurs with a same vertical diffuse attenuation coefficient, then R_B can be approximated by:

$$R_B = R_\infty + (R(0,H) - R_\infty) \exp^{-2KH} \quad (11)$$

where, R_∞ is the reflectance at null depth for the deep ocean, K is an operational diffuse attenuation downwelling irradiance, and H is the depth level. $R(0, H)$ is the reflectance just below the surface of an homogeneous ocean bounded by a reflecting bottom at depth H . For detailed explanation refer to Maritorena *et al.* (1994).

To represent the contribution of the water body, R_{∞} value was derived by selecting a number of deep-water pixels per scene and computing its mean value for each of the spectral bands involved (**Figure 9**). K was replaced by the diffuse attenuation coefficient (K_d) modeled using the Hydrolight 4.1 radiative transfer numerical model (**Figure 10**). Inputs to the code are shown in **Table 8**. Pixel specific depth (H) values come from the bathymetric lidar gridded data.

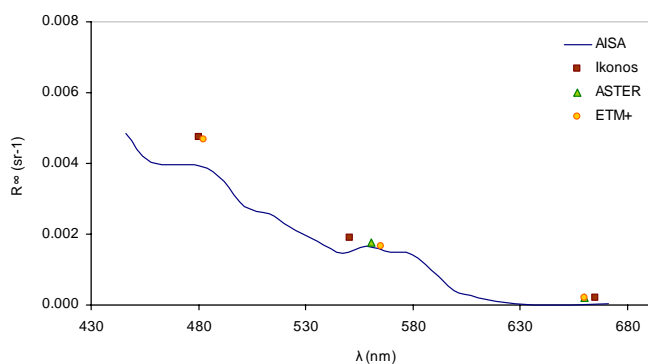


Figure 9. Mean spectra of reflectances measured over deep water (R_{∞}).

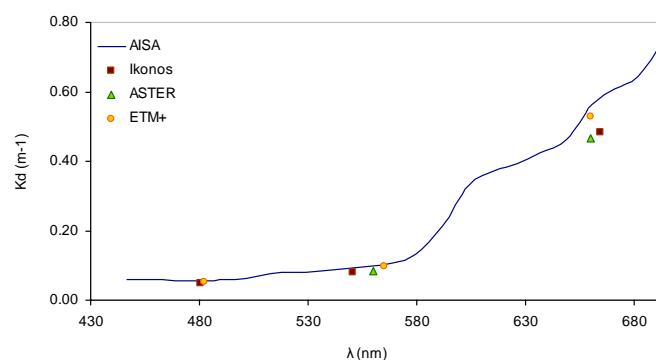


Figure 10. K_d values as estimated with HYDROLIGHT

Table 8. Input parameters for HYDROLIGHT water properties

Parameters	Values
Inherent Optical Property	ABCASE1
Absorption	Pope and Fry's (1997)
Phase function	Pure Water
Typical Chlorophyll	$0.3 \text{ mg m}^{-3} *$
Bb/b	1.2 % *
Sky Model	RADTRAN
Wind Speed	See Table 1
Bottom Conditions	Infinitely deep

* C. Hu personal communication

2.4 Classification Scheme

Even though the study area remains quite the same along the suite of studied scenes, it is very likely that class spectral definition differ according to the spatial characteristics of the capturing sensor (*e.g.* percent coral cover). Most of the reef inhabitants have a spatial extent that is usually smaller than the image pixel size. It means that the spectral value of a pixel carries reflectances of multiple individuals and not just a single unit in the ground. Further, optical remote sensors also capture coral reef structural configuration in two-dimensions. This effect also contributes to the mixture of measured spectral reflectances at pixel level.

The hierarchical classification scheme for Caribbean coral reefs suggested by Mumby and Harborne (1999) was adapted here to allow consistency and comparison between classification results. Regardless the differences between sensors spatial resolution, class definition is based on major benthic habitat constituents and remain quite unchanged throughout the suite of scenes. Therefore, very specific classes only detectable at 1.5 or 4 meters resolution (*i.e.* AISA and Ikonos scale) are omitted to allow a meaningful multi-sensor classification scheme (Capolsini *et al.*, 2003). The quantitative assessments of biotic percent cover and reef community characterization were tabulated based on biological and geomorphological descriptors obtained from the field data sheets.

2.4.1 Geomorphological Structure

Three of the seven geomorphological categories presented in Mumby and Harborne (1999) can be identified within the studied patch reef system. These categories are patch reef, lagoon floor, and reef escarpment. The latter is mainly used to account for the topographic effect at the patch reef side slopes.

2.4.2 Benthic Class Definition

A matrix of Bray-Curtis index of similarity was constructed using a square root transformation, based on *in-situ* data (Bray and Curtis, 1957). Quantitative descriptors were not transformed to maintain the influence of *in-situ* habitat cover percentage throughout the analysis. The field database was first organized per field stations (rows) and variables (columns), and then imported into the PRIMER 5.1 software. The Bray-Curtis index (S_{jk}) is a measure of the distance (similarity) between every pair of sites (jk). A similarity value of 0% means that there is no similarity among a pair of sites, while 100% suggest that the sites are identical. Bray-Curtis ordination was selected given that it has being widely adopted for multivariate analysis in ecology including coral reefs environments. It is also considerate an objective way to statistically categorize complex assemblages of marine communities, as those found in the Caribbean. It is defined as:

$$S_{jk} = \left[1 - \frac{\sum_{i=1}^p |X_{ij} - X_{ik}|}{\sum_{i=1}^p (X_{ij} + X_{ik})} \right] \quad (15)$$

where X_{ij} and X_{ik} are the abundances of the i^{th} “variable” in the j^{th} and k^{th} samples respectively, and p is the overall number of “species”.

To discriminate or distinguish similar benthic classes within the dataset a hierarchical cluster analysis was performed using the average linkage method. This method sorts, hierarchically, the matrix similarity measures into homogeneous groups. Those can then be presented as a tree plot, or dendrogram, for further interpretation.

The categorization of habitats typology was established using the Similarity Percentage (SIMPER) analysis (Clarke and Warwick, 1994). SIMPER provides a measure of the average contribution of each “variable” to the established similarity/dissimilarity. This was applied within assigned clusters to describe habitat type, and among pairs of clusters to define complexity levels within the dataset. For the latter, the average dissimilarity of every pair of cluster combination was examined. The pair with the lower dissimilarity (*i.e.* higher similarity) was merged into a single cluster

following the typology hierarchy. SIMPER was computed to successively merge the clusters until four basic classes were derived (*i.e.* coral, seagrass, sand, algae). The SIMPER analysis was also carried out using the PRIMER software.

2.5 Image Classification

Image classification consists in assigning image pixels to thematic classes based on their spectral properties. This process can be achieved with a variety of methods. The supervised classification approach was embraced here to predict the output benthic habitat classes given collected ground truth data. Supervised classification implies that some *a priori* knowledge of the area of interest allows creating spectral signatures that are used to train the algorithm. Here, the conventional maximum likelihood (ML) classifier was applied. The ML decision rule is considered to be robust given that its estimation depends on the covariance between spectral bands for each of the classes. This algorithm has also been widely used by reef remote sensing scientists in similar studies.

2.5.1 Data Training

Training pixels were defined based on visual image interpretation, with the guidance of field descriptions and videography collected *in-situ*. Pixels of well known ground areas were selected as training sites. The spectral signature separability of those was compared with the spectral signatures of correspondent *in-situ* data for quality control. The benthic class typology was assigned following the classification scheme as defined in section 2.4. Same training areas were identified for AISA and Ikonos.

To visually gather training pixels for the lower spatial resolution images ASTER and ETM+ was more challenging because of the increased spectral mixing. To aid with the definition of training pixels for the coarser resolution images, it was necessary to interactively evaluate the spectral signature and geographic location of individual pixels (sites) over the higher resolution Ikonos image.

It is desirable that habitat signatures derived from training samples are representative of the class in question and dissimilar to other classes. Therefore, pixels that presented abnormal signatures were carefully examined (*e.g.* dark for sand, bright for dense seagrass). The ML algorithm assumes normality within the training data, and such parametric rule should be approximated by having an appropriate sample size and by checking for deviated spectral values within the samples. The inter and intra classes spectral distances based on the spectral separability report derived from Jeffries-Matusita and Transformed Divergence (ENVI®) separability measures (Richards, 1999) was examined. Once the statistical characterization was approximated the image classification approach followed using the ML decision rule with equal probabilities of the classes. Same training signatures were applied to classify the L , R_{rs} , R_B , and Y_{ij} images per sensor (*i.e.* radiance, remote sensing reflectance, bottom remote sensing reflectance, and invariant bottom index, respectively).

2.5.2 Control Data

The same study area was considered to test the classification accuracy of the different sensors (**Figure 11**). Given the different number of pixels constituting each sensor image, the number of control sites per image was not the same (Stehman, 1997; Capolsini *et al.*, 2003). The ground truth data was used to specifically test the accuracy of AISA classification results for L , R_{rs} , R_B , and Y_{ij} images.

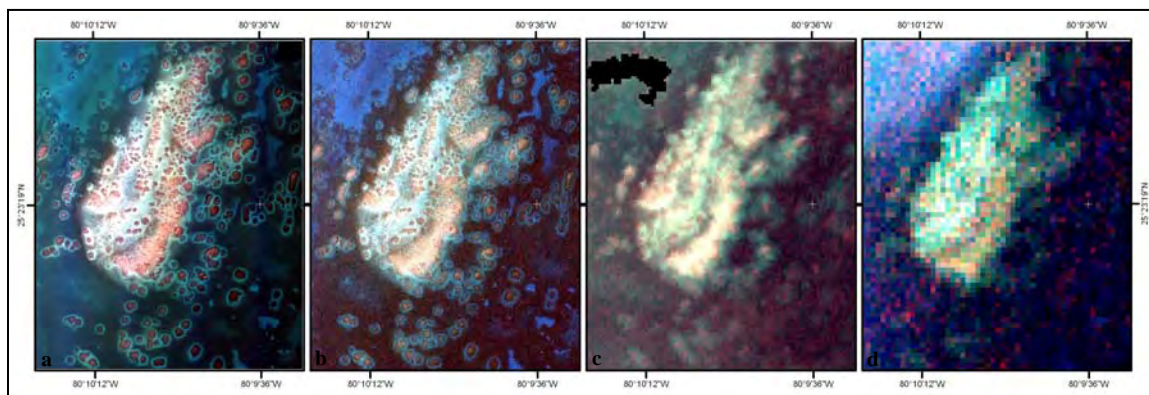


Figure 11. Images of the study area represented using an RGB color composite. a) AISA with bands 14, 8, and 2; b) Ikonos with bands 3, 2, and 1; c) ASTER using band 2, 1, and 1; d) ETM+ with bands 3, 2, and 1.

The number of control points or ground truth sites was adequate to test the overall classification accuracy of AISA and Ikonos. However, because of the coarser resolution of ASTER and ETM+, it was necessary to discard a number of control sites (*i.e.* 12 and 25 for ASTER and ETM+ respectively). The reduced set was too limited to represent or assess the accuracy of some benthic classes for the latter images. To deal with such situation, AISA was considered a ground-truth image from which control pixels were generated. For consistency, same strategy was applied to generate a number of control points proportional to the number of pixels in every spaceborne image evaluated. The selection of control pixels, with AISA as master, was achieved by the following steps:

1. Resample the classified AISA image, after assessing its classification accuracy (*see* section 2.5.3), to the different spatial resolutions of the spaceborne images (*i.e.* 4, 15, and 30 meters).
2. Generate a stratified random sample over the corresponding AISA classification map proportional to the size of each thematic class.
3. Derived control pixels are exhaustively tested over the actual AISA image and resulting thematic maps to better approximate ground truth.
4. Reconcile control pixels to the correspondent spaceborne image and proceed with the accuracy assessment.

2.5.3 Accuracy Assessment

The percentage agreement of classified habitat maps was assessed using the overall, user, and producer accuracies computed from the derived confusion matrices. The overall accuracy (\mathbf{P}_o) is the proportion of the correctly classified and total number of control points. User's accuracy (\mathbf{P}_u) is the ratio of correctly classified control point and total number of control points per row, the lower the user's accuracy the more error of commission. While producer's accuracy (\mathbf{P}_p) is found by dividing the correctly classified control point by the total number of control points per column, the lower the producer's accuracy the more error of omission. The two latter measures show the classification accuracy of individual classes (Congalton, 1991).

We also evaluate the *Tau* coefficient of accuracy (T) as a complementary measure to P_o . This coefficient, unlike to the overall accuracy, also accounts for the omission and commission errors (*i.e.* off-diagonal values) in the confusion matrix. It measures the improvement of a classification over a random assignment of pixels ($T=0$) (Ma and Redmond, 1995). It is calculated from:

$$T = \frac{P_o - P_r}{1 - P_r} \quad (16)$$

where

$$P_r = \frac{1}{N^2} \sum_{i=1}^M n_i \cdot x_i \quad (17)$$

(*i.e.* N = the total number of control sites, M = number of classes, i = is the i th classes, n_i = row total of class i , x_i = diagonal value for class i). Assuming a distribution close to normality, then a Z-test can be performed to check over the differences of two Tau coefficients (Ma and Redmond, 1995). The Z-test between Tau coefficients is:

$$Z = \frac{T_1 - T_2}{\sqrt{\sigma_1^2 + \sigma_2^2}} \quad (18)$$

where the variance of Tau is

$$\sigma^2 = \frac{P_o(1-P_o)}{N(1-P_r)} \quad (19)$$

and T_1 and T_2 are the coefficient of two independent confusion matrices. A Z-test greater than zero at the 95 percent significance level ($Z \pm 1.96$) would agree with the null hypothesis H_0 ($T_1 = T_2$), otherwise it would favor the alternative hypothesis H_1 ($T_1 \neq T_2$) (Ma and Redmond, 1995).

Chapter 3

3. Results

3.1 Performance of image correction methods

3.1.1 Atmospheric Modeling

Image classification results for images with radiance and R_{rs} values were compared to account for any major changes. Classification results were significantly similar. From here on then R_{rs} images are considered the base images for comparison.

Image classification results of Ikonos (R_{rs}) before and after glint correction were also compared. Results consistently show an increased overall accuracy ranging from 2 up to 7% on the image maps derived from the glint corrected values. The glint corrected Ikonos image (R_{rs}) is the one used for further image processing and accuracy assessment comparisons.

3.1.2 Bathymetric Correction

Visually, bathymetric correction was effective by enhancing the contrast between the lagoon floor habitats. In the case of the R_B images, deep sand pockets, seagrass and reef patches showed a spectral signal more alike to those on shallower waters. Spatial details, like changes in lagoon floor seagrass densities, also become clearer. Both algorithms produced considerable enhancements when inspecting the resulting images. That is especially the case for AISA and Ikonos as seen in **Figure 12**. ASTER, also presents a remarkable enhancement of the bottom floor on the R_B image but not the Y_{ij} one. The benefits of water column correction are not very obvious for ETM+ (**Figure 13**).

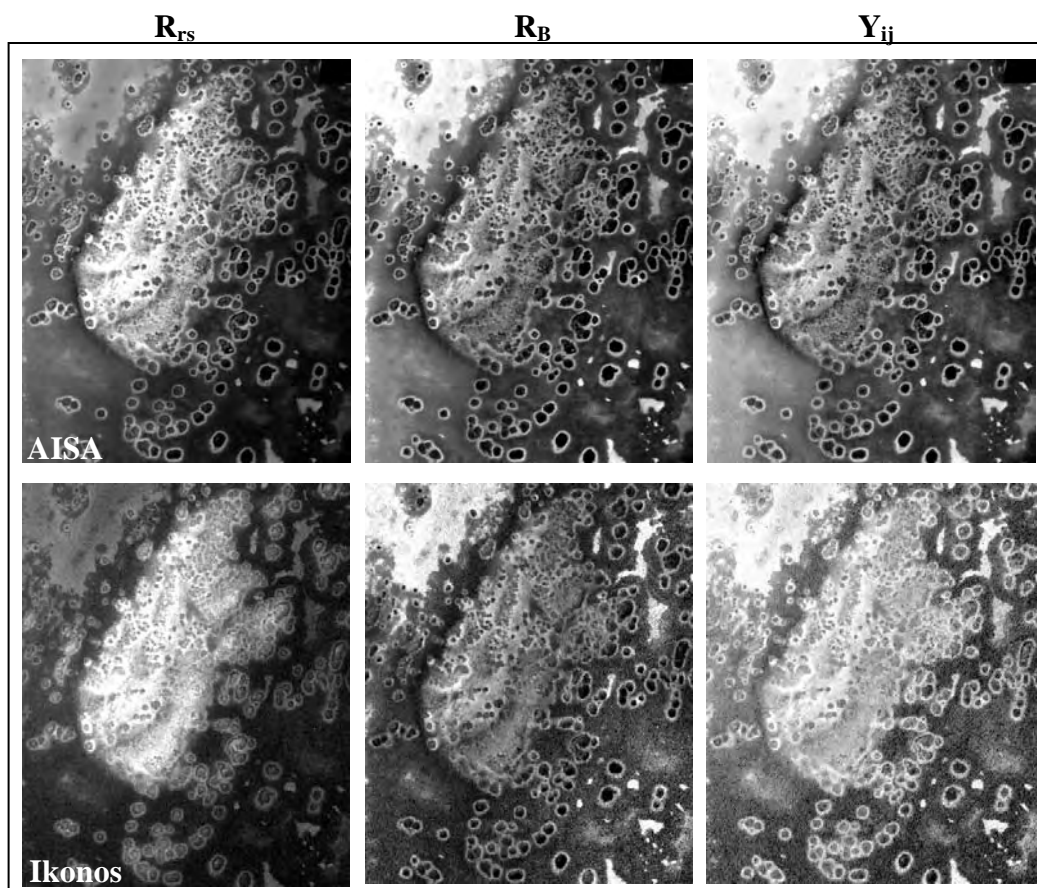


Figure 12. Visualization of AISA (top) and Ikonos (below) images before and after water column correction. Images are represented using the single band 5, and band ratio b6/b9 for AISA, and band 2 and band ratio b1/b2 for Ikonos.

Six depth invariant bands were created for AISA, and three for Ikonos and Landsat respectively. ASTER, with only two water penetrating spectral bands, produced a single depth invariant index band. Thus, multispectral classification could not be performed on this single band since the classification algorithm adopted (*i.e.* maximum likelihood) requires two or more image bands to produce the statistics necessary for spectral habitat separation. This limited the possibility of assessing the benefits of the empirical Lyzenga's model over ASTER.

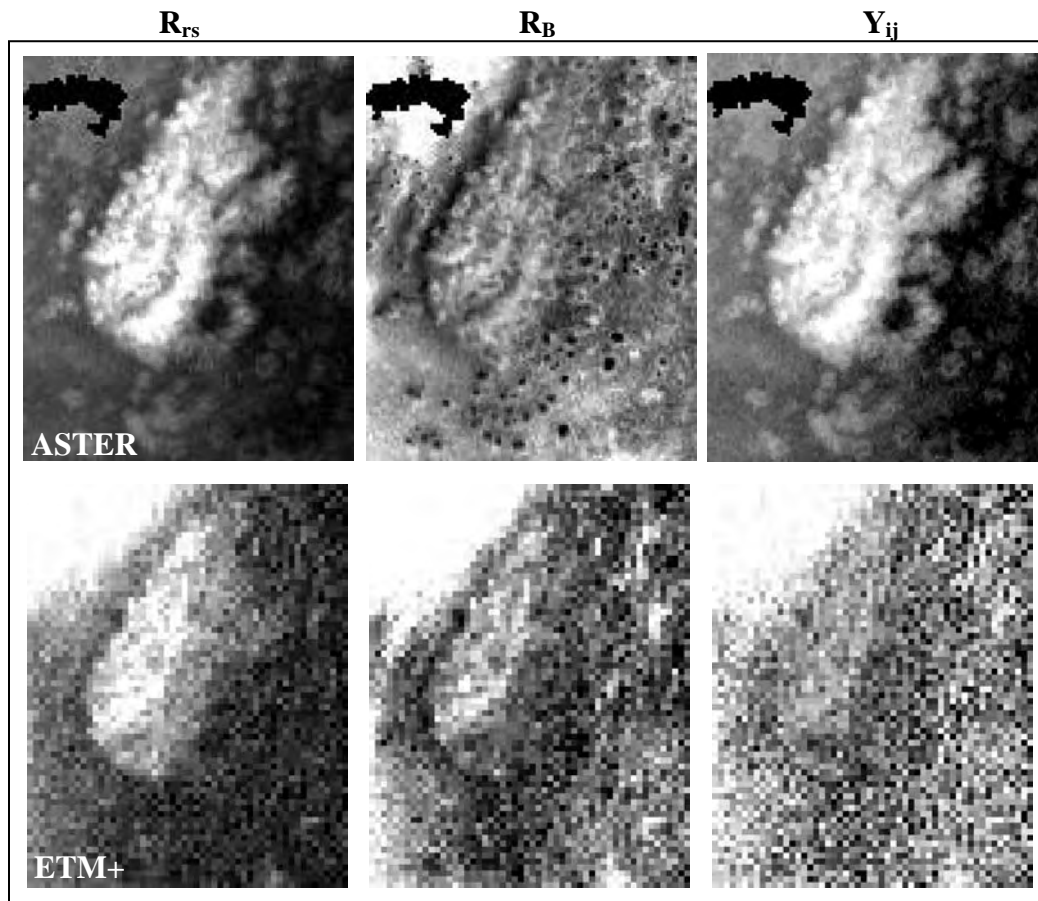


Figure 13. Visualization of ASTER (top) and ETM+ (below) before and after water column correction. Images are represented using band 1, and band ratio b1/b2 for ASTER and ETM+ respectively.

3.2 Determination of Habitats Classification Scheme

Cluster analysis was used to group field data into habitat classes based on the Bray-Curtis similarity matrix (**Figure 14**). The hierarchical classification suggested 10 classes at a fine descriptive resolution (**Figure 15**), while higher up in the hierarchy four basic coarse classes (*i.e.* coral, algae, seagrass, sand) can be defined. Each complexity level was derived starting at the fine level of class definition. Then, a SIMPER analysis was employed to determine the contribution of the linked sites to the hierarchy and for label assignment (*i.e.* accounting for the more dominant benthos per class).

Class definition similarity values at the fine descriptive level ranged from 60 to 99 percent. These numbers represent the degree of uniformity among the factors defining each benthic class. The coral classes obtained the lower values (*i.e.* 60 to 67 percent), and indeed those are the classes with the more heterogeneous substrate type. Classes dominated with seagrass, algae, and sand reached the higher values (*i.e.* 72 to 99 percent) suggesting more synonymous classes. Habitat typologies at a coarse level (*i.e.* coral, seagrass, algae, sand) are achieved at a threshold of about 55 percent similarity. Sand and algae are well differentiated at the level of 52 percent. However, it is important to note that only four field sites (*i.e.* two each) are use to describe these classes. The major discriminative contributors for the class coral include gorgonians, algae, and coral rubble. Gorgonians are the most prominent of all with a 30 to 46 percent contribution to the *dense live covered substrate* class. Scattered stony corals only contributed a 4 to 11% to

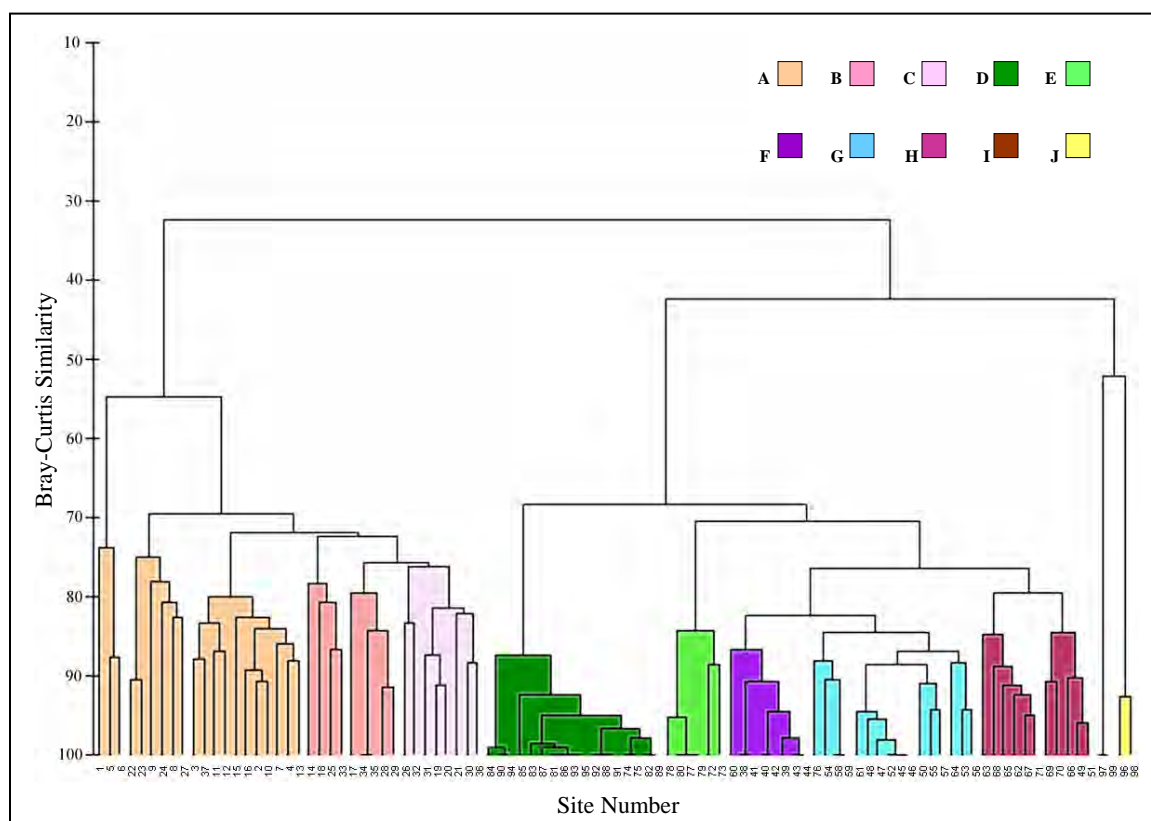


Figure 14. Cluster diagram, or dendrogram, showing the similarity of habitat communities among sampled sites. Colors represent class definition grouping at the fine complexity level. Refer to Table 9 for the description of habitat classes.

Table 9. Interpretation of benthic communities at coarse and fine complexity levels as derived from the Bray-Curtis analysis. Labeling letters corresponds to the color coding indicated in Figure 14. Habitat percentage cover and geomorphological attributes were incorporated in the classification scheme following habitat definition as presented by Mumby and Harborne (1999).

Coarse Complexity		Fine Complexity	Characteristics
Habitat Label		Habitat Label	
Coral Classes (>1% hard coral cover)	A	Dense live covered substrate	More than 50 percent is life-covered substrate. Including hard coral, gorgonians, benthic algae, sponges and seagrass. Mainly over patch reefs.
	B	Dense live covered reef edge	Similar to class A, mainly with more abundant gorgonians, dead coral and coral rubble. Sitting at the patch edge or escarpment, with a slope averaging 25 degrees.
	C	Sparse live covered substrate	Less than 50 percent is life-covered substrate. Predominantly bare substratum (pavement, dead coral, coral rubble, sand pockets). Over patch reefs.
Seagrass Dominated (>10% seagrass cover)	D	Dense seagrass	More than 70 percent total cover. Individual or mixed beds of <i>Thalassia</i> and <i>Syringodium</i> with scattered occurrence of calcareous green algae. On the lagoon floor.
	E	Medium density seagrass on sandy bottom	Cover 30 to 70 percent. Individual or mixed <i>Thalassia</i> and <i>Syringodium</i> , over clean carbonate sand. On the lagoon floor as patch reef halo.
	F	Sparse seagrass	Less than 30 percent cover. Usually <i>Thalassia</i> over carbonated sand with some occurrence of calcareous green algae. On the lagoon floor in a matrix of clean carbonate sand.
	G	Medium density seagrass on sandy bottom with algae and coral rubble	Cover 30 to 70 percent, mainly <i>Thalassia</i> with very sparse patches of sponges, gorgonians, algae, and coral rubble. On the lagoon floor.
	H	Seagrass with distinct coral patches	Seagrass visibly dominant, with sparse occurrence of gorgonians, algae, sponges, coral rubble or small stony corals.
Algal dominated (>50% algal cover)	I	Algal dominated	10 to 50 percent cover of brown and calcareous algae. On the deep lagoon floor over a matrix of mixed carbonate sand and mud.
Bare substratum	J	Sand	Carbonate sand/mud with occurrence of sparse green algae and/or seagrass.

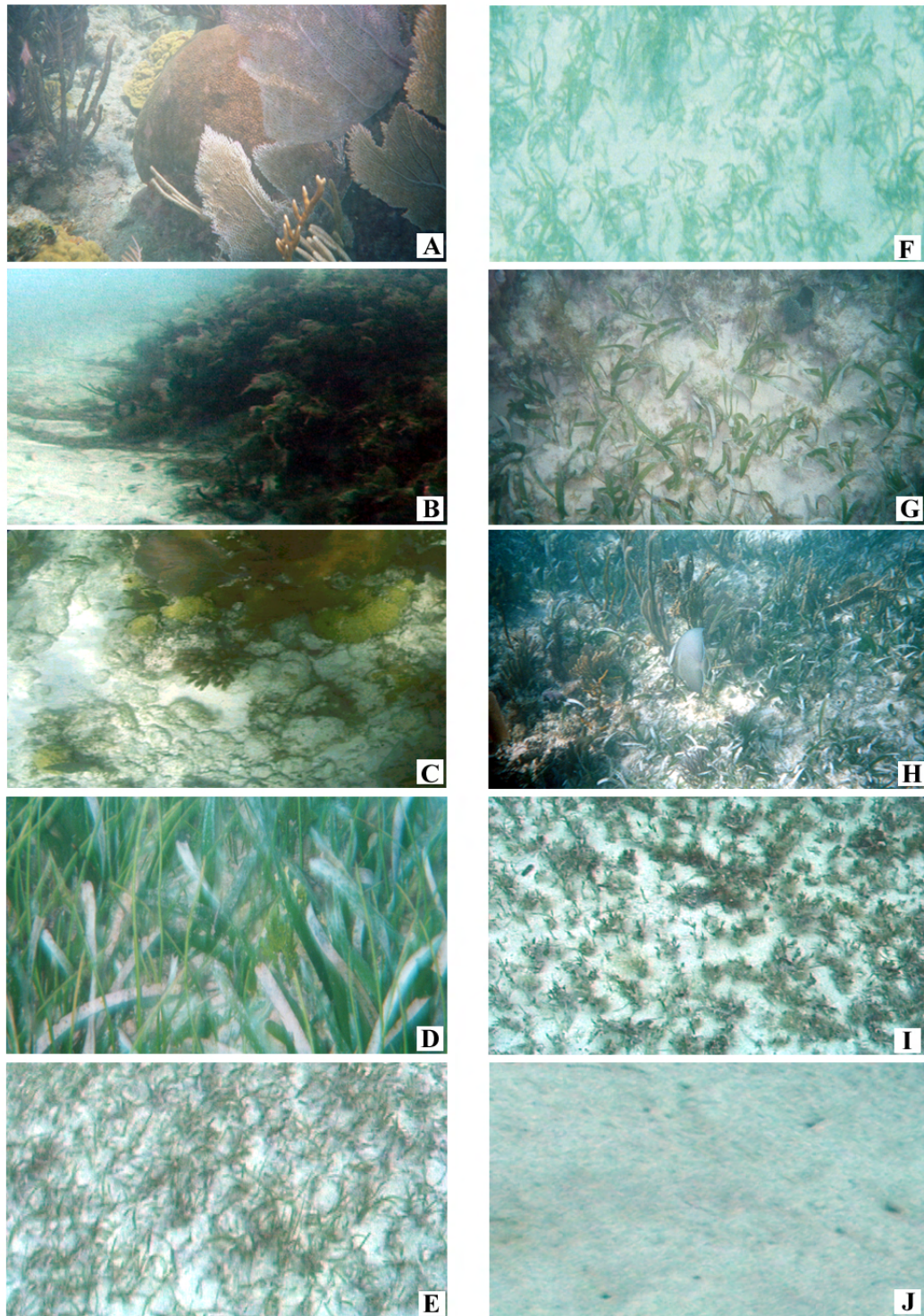


Figure 15. Illustrations representing the different habitat categories used in the classification scheme at a fine complexity resolution. Benthic and geomorphological components (*i.e.* patch reef, reef edge, and lagoon floor) are embedded within the classification descriptors. Refer to Table 9 for class description.

the same class. For the seagrass class, seagrass was the major contributor except for the sparse seagrass class where a sandy background is usually dominant. Five seagrass classes were derived from the hierarchical classification. Those are mainly differentiated by a quantified estimate of percent cover. Habitat classes at a fine complexity level were merged into more generalized habitats as in **Figure 16**.

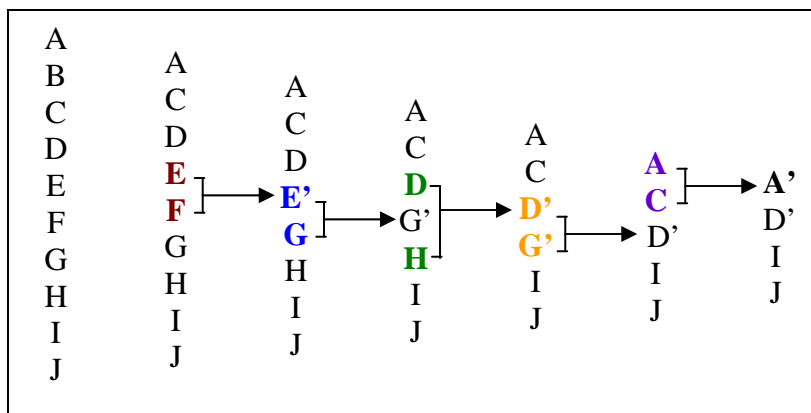


Figure 16. Diagram showing pair of classes consecutively merged at individual SIMPER analysis runs.

3.3 Image Classification Analysis

A total number of 105 habitat maps with correspondent confusion matrices were generated for analysis. That is, seven images for each of the four sensors accounting for the seven levels of habitat complexities, multiplied by the four different image-processing stages, including L . An exception to that is ASTER, which was not processed to Y_{ij} .

3.3.1 Comparison between Sensors

Overall, AISA was consistently more accurate than the other satellite sensors (**Figure 17a**). The accuracy achieved by AISA remained significantly high throughout the analysis ($> 85\%$) for every habitat complexity levels. From the intermediate complexity level of 7 classes to the coarser level of 4 classes AISA P_0 did not change significantly, showing values ranging from 94 to 97%. The image classification accuracy of AISA was contrasted to those of other satellite sensors by differences in pairs of Tau coefficients (z-test) (**Table 10**). At a 95% significance level, z-test reveals significant

differences between the digital airborne high spectral image (AISA) and the broader spatial and spectral spaceborne images. Ikonos is the only satellite sensor that shows some correspondence to AISA. However, such correspondence is only reached at the coarse complexity levels of 5 and 4 habitats. **Figure 18** shows the classification maps at the different habitat complexity levels as derived from the AISA image.

Ikonos overall accuracy results show a clear trend of higher accuracy for lower habitat complexities (**Figure 17b**). Overall accuracies ranged between 55% at 10 habitat classes to 85% at 4 habitats regardless of the image processing method. Z-tests among pairs of Tau coefficients do not suggest a correspondence between this high spatial resolution sensor to the coarse spatial resolution ASTER and ETM+ (**Table 10**). After bathymetric correction (R_B), however, all sensors showed correspondence with Ikonos for the habitat classification schemes containing only 5 and 4 classes. There is a marked significant difference between all sensors after Y_{ij} water column correction.

ASTER presents a similar but weaker trend of increasing accuracy with decreasing habitat complexity (**Figure 17c**). However, such trend is considerably more apparent for the image processed to R_B compared to the lower stage of image processing R_{rs} . ASTER proved to be significantly different to AISA and Ikonos, but similar to ETM+ at every level of habitat complexity ($0.04 < Z < 1.86$) (**Table 10**). For R_{rs} , overall accuracy shows a slight increase between 10 and 4 habitat classes, with values ranging from as low as 36.75% to a moderate 54.78% respectively. In contrast, R_B produced overall accuracy values going from 51.20% to 82.17% for the same habitat complexities. The Tau coefficient, however, remained relatively low for both image-processing cases ($< 52\%$).

Table 10. Z-test results comparing the significant difference between Tau coefficients for the four sensor images processed to (a) R_{rs} , (b) R_B , and (c) Y_{ij} at seven habitat complexities. Values in bold denote a significant difference between pair of sensors.

No. Classes	AISA:Ikonos	AISA: ASTER	AISA:ETM+	Ikonos:ASTER	Ikonos:ETM+	ASTER:ETM+
10	4.58	6.28	-	2.48	-	-
9	3.93	5.63	5.74	1.89	2.07	0.22
8	2.63	5.19	4.76	2.25	1.81	0.59
7	2.98	5.17	5.17	3.11	3.11	0.03
6	3.19	5.61	5.88	3.44	3.90	0.47
5	1.64	4.20	4.47	3.15	3.53	0.33
(a) 4	1.65	4.19	3.30	3.04	1.92	1.24

No. Classes	AISA:Ikonos	AISA: ASTER	AISA:ETM+	Ikonos:ASTER	Ikonos:ETM+	ASTER:ETM+
10	3.71	5.03	-	1.83	-	-
9	2.47	4.02	5.41	2.03	3.24	1.13
8	2.92	3.77	5.18	1.25	2.34	0.94
7	2.44	4.13	5.50	2.30	3.31	0.89
6	2.84	4.38	5.86	2.15	3.15	0.78
5	1.71	2.52	4.39	1.11	1.79	0.37
(b) 4	1.73	2.66	3.87	1.13	1.70	0.34

No. Classes	AISA:Ikonos	AISA:ETM+	Ikonos:ETM+
10	3.48	-	-
9	2.30	5.40	4.09
8	2.95	5.16	3.06
7	2.95	5.57	3.83
6	3.34	5.87	3.81
5	2.14	4.54	3.02
(c) 4	1.97	3.87	2.34

As ASTER, ETM+ reproduced an increasing but quite ambiguous trend of overall accuracy improvement towards the coarse habitat schemes for image processed to R_{rs} . Overall accuracies go from 47.33% for 9 classes to 63.33% for 4 habitat classes, with a drop in accuracy between intermediate habitat schemes. A similar situation is apparent for the Y_{ij} image maps. However, the latter did to not increase the classification accuracy over the more basic processing level R_{rs} . In general, higher accuracy values for ETM+ are obtained with R_B (49.33% to 68.67% for 9 and 4 habitat classes respectively) relative to the other image processing methods. Based on the z-test, ETM+ only presented some correspondence with ASTER.

Z-test values for Y_{ij} (Table 10c) present a marked significant difference among all the sensors. This was expected since the Y_{ij} method produce a unitless bottom-index that lack spectral information, and resulting indexed band values are not spectrally related.

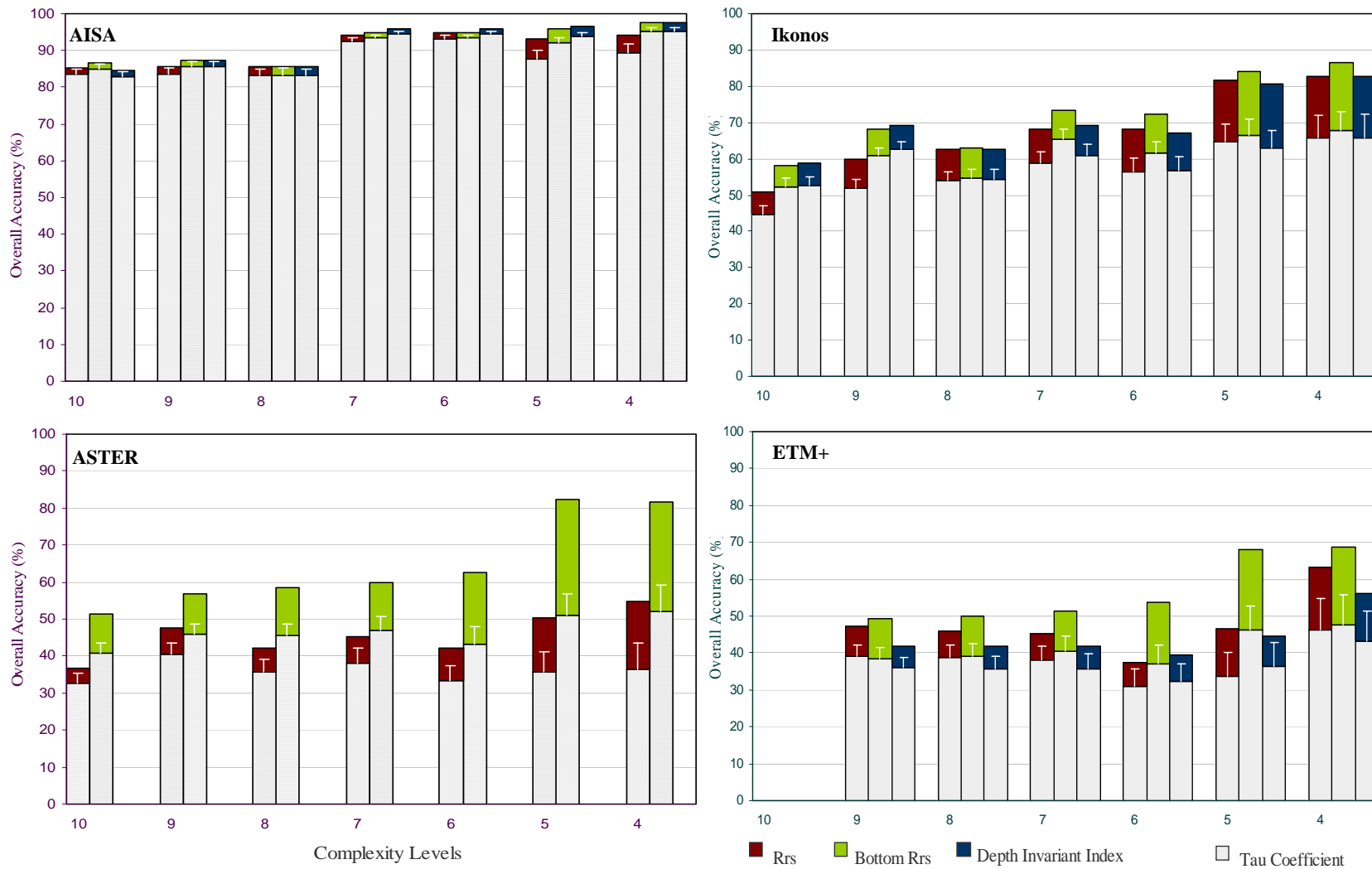


Figure 17. Comparison of overall accuracy and Tau coefficients for the classification of four sensor images at seven levels of habitat complexities (Error bars are the upper 95% confidence intervals of Tau coefficient). The three different values denote the influence of different stages of image processing.

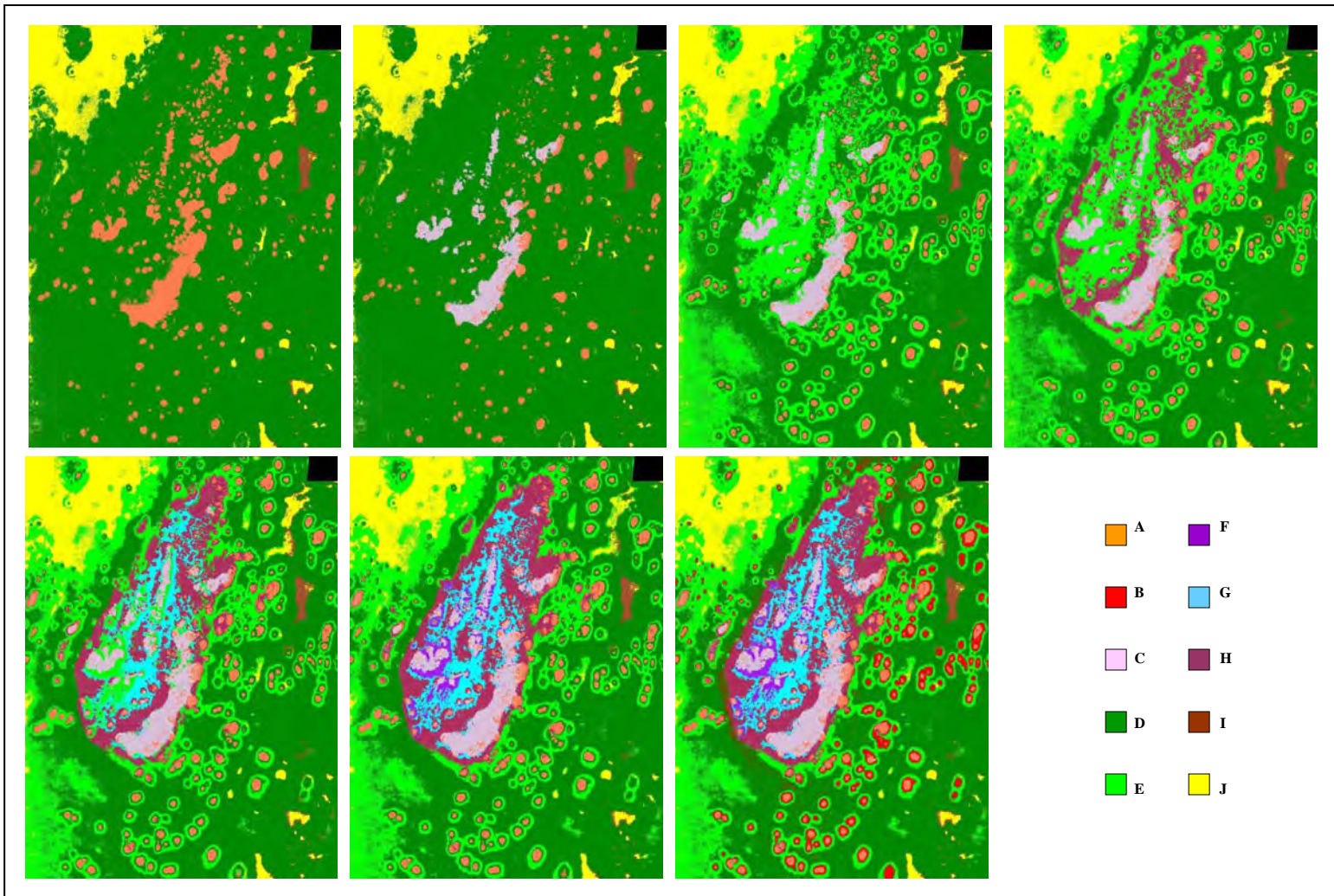


Figure 18. AISA based image maps derived from a supervised classification of remote sensing bottom albedo values. Each map represents a different habitat complexity. From top-left: the coarser complexity (4 classes) going towards the finer complexity (10 classes) at the bottom-right. Color coding represents habitat classes as described on table 9.

3.3.2 Comparison between Methods

Same training and control pixels were employed for the supervised classification of individual image data that undergoes three different levels of image processing.

After confirming a significant agreement in the overall accuracy of total radiance and R_{rs} images, the latter became the basis for comparison. In all the cases R_{rs} returned lower overall accuracies when compared to R_B . Comparison between R_{rs} and Y_{ij} , however, do not always show such a clear pattern.

Successfully employed in previous studies (Armstrong, 1993; Mumby *et al.*, 1998), here the empirical Y_{ij} method yielded variable results among the different sensors. For AISA Y_{ij} performed relatively well, only differing to the already high R_{rs} P_o values by $\pm 3\%$. For the complexity levels of 7, 6, and 5 this processing method even returned higher accuracies than those attained by R_B . Ikonos results at habitat complexity levels 9 and 10 showed a more obvious tendency to improved accuracy by Y_{ij} . However, at coarser habitat complexities the P_o of Y_{ij} balances up with R_{rs} values, suggesting no improvement. It is immediately apparent that this empirical method performed poorly for ETM+. For the latter, Y_{ij} consistently presented lower accuracies than those attained by R_{rs} .

R_B image processing stage introduced a relatively slight improvement to AISA's overall accuracy when compared to R_{rs} . Again, for AISA, all the three image processing methods returned significantly high accuracies. Thematic maps derived from R_B using the very detailed bathymetric DEM returned superior overall accuracies for all the satellite sensors. ASTER is the one that shows the higher proportion of benefits from the R_B method in comparison to the other sensors. The overall accuracy gained by this sensor at 5 habitat classes reached an improvement of 32% over the R_{rs} . From the z-test values (Table 11), it appears that despite the different responses, the three methods are not necessarily significantly different between each other for all of the sensors.

Table 11. Z-test results comparing the significant difference between the classification of (a) AISA, (b) Ikonos, (c) ASTER, and (d) ETM+ images processed with three different methods at seven habitat complexities. Values in bold denote a significant difference between pair of methods.

	No. Classes	Rrs:RB	Rrs:Yij	RB:Yij
(a)	10	0.15	0.07	0.22
	9	0.18	0.18	0.00
	8	0.01	0.00	0.01
	7	0.08	0.16	0.08
	6	0.16	0.16	0.00
	5	0.26	0.37	0.10
	4	0.34	0.34	0.00
(b)	10	1.27	1.31	0.04
	9	1.24	1.46	0.21
	8	0.09	0.05	0.05
	7	0.79	0.25	0.54
	6	0.64	0.05	0.61
	5	0.16	0.15	0.30
	4	0.17	0.00	0.17
(c)	10	1.54	-	-
	9	0.85	-	-
	8	1.56	-	-
	7	1.30	-	-
	6	1.42	-	-
	5	1.33	-	-
	4	1.34	-	-
(d)	10	-	-	-
	9	0.13	0.61	0.85
	8	0.05	0.56	0.58
	7	0.42	0.44	0.83
	6	1.05	0.27	0.82
	5	1.59	0.50	1.24
	4	0.14	0.39	0.51

3.3.3 Discrimination of Habitat Classes

Although the study area is relatively small and some of the classes are also spatially small, the accuracies (user and producer) of individual habitat classes cannot be rigorously discussed considering the reduced number of reference points describing benthic classes (Cogalton, 1991). However, it is possible to depict some general trends from the omission and commission errors as derived from the resulting error matrices

(Table 12 and 13). For AISA, most of the habitat classes were relatively well resolved at every complexity and image processing level. The satellite sensors, however, showed a contrasted response with significant confusion discriminating most of the individual classes. In general, the *dense seagrass* class seems to be the one that was relatively better resolved. Most of the classes' poor discrimination or confusion relates to the degree of spatial patchiness and variability of each benthic habitat class per image spatial resolution. (**Figure 19**).

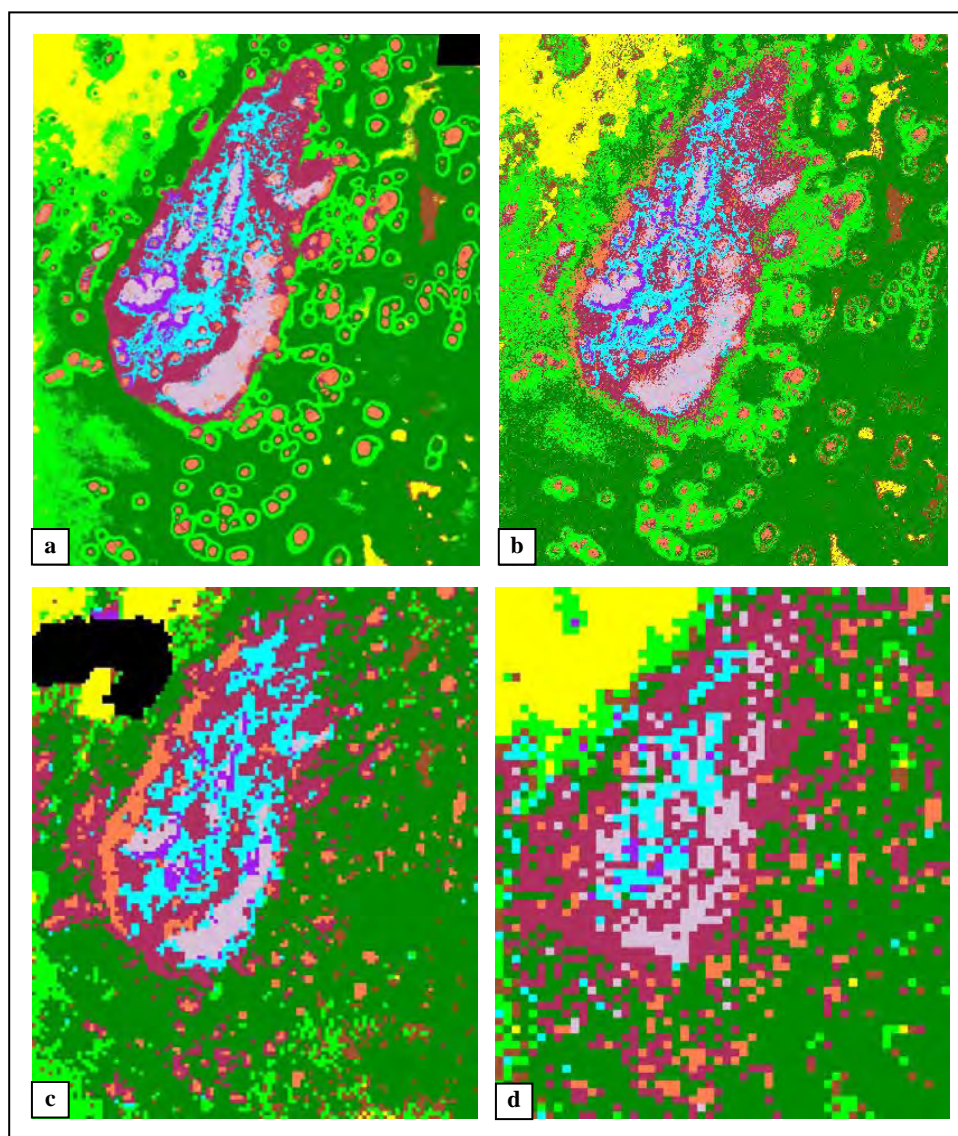


Figure 19. Image derived thematic maps for nine habitat classes visually showing the relative difficulties for the spaceborne sensors to discriminate spatially small and patchy features. Illustration shows AISA, Ikonos, ASTER, and ETM+ R_B images (a, b, c, and d respectively).

Chapter 4

4. Discussion

4.1 Spectral, Spatial, and Descriptive Resolutions

The configuration of the high spectral and spatial resolution AISA sensor rendered significantly better results compared to the other satellite sensors. Overall accuracy of AISA delivered values as high as 84% for fine complexity habitat mapping, reaching a higher P_o of 95% at a coarse habitat complexity level. The relative high accuracy attained by AISA was maintained along the analysis for the different habitat complexities considered here. These results compared favorably with those reported by Mumby *et al.* (1998b) for a similar airborne hyperspectral imager system (CASI). They obtained P_o values ranging between 70 and 90% for fine to coarse habitat schemes for a fringing reef environment in the Caribbean. These results confirm the higher potentiality of an effective combination of high spectral and spatial resolution in the degree of accuracy gained for coral reef habitat mapping relative to that offered by satellite sensors. However, there are several aspects such as cost, availability, geographic coverage, and historic temporal resolution, which lead the reef scientific community to keep exploring the potentialities of available spaceborne images for marine studies.

Significantly varying in both spatial and spectral resolution, the satellite sensors rendered considerable discrepancies for benthic habitat classification relative to AISA. Several trends in map accuracy have suggested that, given the low spectral contrast between reef habitats delivered by spaceborne sensors (Hochberg and Atkinson, 2003a), the more significant aspect to consider for better accuracy relies then on the sensor's spatial resolution (Capolsini *et al.*, 2003, Mumby and Edwards, 2002). The results of this study support such premise following a similar trend of higher classification accuracy (*e.g.* about 10%) gained by the higher spatial resolution Ikonos over ETM+. This two sensors share very similar spectral resolution but differ considerably in spatial resolution (*e.g.* 4m and 30m). Results for ASTER classification accuracy however, did not showed advantage over ETM+ even when the former has a higher spatial resolution (*e.g.* 15m and

30m). Actually, in most cases, ASTER performed poorly relative to ETM+. These results go in agreement with those presented by Capolsini *et al.* (2003). The more likely explanation to this resides on the less suited spectral attributes of ASTER, having only two water penetrating bands, for coral reef mapping. Mumby *et al.* (1998b) compared classification accuracies of high-spatial but low-spectral resolution aerial photography to those of CASI (*e.g.* high-spectral and high-spatial resolution), and results favored the latter over aerial photography. Although, the compared case study areas and mapping approach for CASI and aerial photography were not totally comparable, the aforementioned suggests that spatial and spectral resolution should complement each other, given that sacrificing one of them implies reducing effectiveness to the other. By all means then Ikonos is favored over ASTER and ETM+ satellite sensors, spatially and spectrally, by proving higher accuracy for reef habitat mapping (Figure 17). ASTER and ETM+ were not effective for fine level habitat mapping ($P_o < 50\%$) over the patchy coral reef case study area.

Results for the four sensors considered here (*i.e.* AISA, Ikonos, ASTER, ETM+ ETM+), and others evaluated in previous studies (*i.e.* CASI, MASTER, Landsat TM, Landsat MSS, SPOT XS, and SPOT Pan) (Andréfouët *et al.*, 2003c; Capolsini *et al.*, 2003; Mumby and Edwards, 2002; Mumby *et al.*, 1998b), shows clearly that the number of mapped thematic classes is in linear relation to the accuracies gained in the classification. Such statement is also readably confirmed in this study, with some exceptions that are discussed in section 4.3.

4.2 Image Processing and Classification Accuracy

Overall, AISA did not showed significant difference in P_o considering the three different levels of image processing and each level of habitat complexities. A slight improvement (~3%) in AISA classification accuracy is depicted by means of bathymetric correction. However, there is no clear trend in which of the applied methods (R_B , Y_{ij}) performed better. Contrasted results to these were obtained in Mumby *et al.* (1998a)

where an airborne multispectral CASI image obtained a 13% improvement in P_o after applying the empirical Lyzenga's model at a fine descriptive resolution. The more likely reason for such difference is that our study site comprises depths less than 12m, while depths in Turk and Caicos study reached a maximum of 20m. Turk and Caicos study also reported no significant improvement in P_o for CASI after water-column correction (Y_{ij}) for habitat mapping at coarse descriptive resolution. AISA proved its potential regardless further image processing.

Ikonos P_o only improved by 5% after R_B correction. It did not improved significantly however after Y_{ij} correction. Of all four sensor evaluated here, ASTER is the one showing a remarkable recovery in P_o with the addition of detailed lidar bathymetric data for water-column correction (R_B). R_B image processing rendered accuracies almost 30% higher than the ones obtained from R_{rs} alone. After such correction, the enhanced spatial resolution of ASTER revealed its superiority over the 30m ETM+ by producing values about 10% higher than those for ETM+. Further, at habitat complexities of 4 and 5 classes ASTER even reached P_o values more similar to Ikonos, although its Tau coefficient remained quite low ($T = 51\%$) and comparable to those of ETM+. This study is first presenting the R_B method with detailed lidar bathymetric data for coral reef mapping. Thus, further inter-site comparison is not possible at this point.

The results of this study showed relative improvement from bathymetric correction for all the images. Among the image processing methods considered, R_B demonstrated to be the one that performed better increasing mapping accuracy. The Y_{ij} method does not present significant improvement for AISA or Ikonos and performed poorly over ETM+. Part of the Y_{ij} low performance can be explained by the difficulties finding a unique substrate type well represented at different depths in the studied scenes, situation that is certainly accentuated with coarser spatial resolutions. A recent study (Purkis and Pasterkamp, 2004) presents remarkable benefits from water depth corrections to in-situ above-water spectra used as a basis for the classification of a Landsat TM image. Although different image classification protocols, the water column corrections

methods adopted in their study (Bierwirth *et al.*, 1993) compares to this study R_B approach. They favored the method and recommend coupling bathymetric data to in-situ optical measurements to correct for the effect of the water-column and improve classification accuracy of Landsat imagery.

It is not clearly depicted here that the benefits gained by water column correction are more apparent at finer habitat complexities as suggested by Mumby *et al.* (1998a). Only the Ikonos images R_B and Y_{ij} showed a weak trend suggesting so, relative to R_{rs} . However, ASTER and ETM+ gained the more benefits from water column correction (R_B) compared to AISA or Ikonos.

4.3 The Reef Environment and Classification Scheme

The studied area encompasses a number of individual small reef patches scattered over a shallow lagoon basin covered by seagrass with perceptible spatial changes in densities. Seagrass spatial changes are not expected to change significantly within the scenes timeframe. Once again, AISA proved to be capable of mapping most of the narrow geomorphological features and differences in seagrass densities present in this patch reef lagoonal system (**Figure 18**). On the other hand, the class *dense life covered reef edge* immediately appeared not suited for any of the satellite sensors. It is actually possible to visually recognize the existence of such class at Ikonos and ASTER resolutions. However, given the spectral challenges introduced by the topographic slope, neither Ikonos nor ASTER were efficient to spectrally discriminate it from the surrounding seagrass beds. For ETM+, this spatially narrow class was quickly discarded because of resolution constrains.

Thematic maps derived from ASTER and ETM+ showed a tight range difference in overall accuracy and Tau coefficients ($\pm 5\%$) between habitat complexity levels 9 thru 6, and within the different stages of image processing. The fairly constant low P_o could be interpreted as a limitation of those broadband sensors to spectrally discriminate

between seagrass with variations in density. By considering the landscape, it is also reasonable suggesting that the baseline map accuracy is modulated by the seagrass spatial patchiness relative to the capturing spatial resolutions (15 – 30m). Both points are valid. Then, it may seem pointless to keep paying attention to results showing such a poor performance ($P_o < 56\%$). These observations, however, helped putting this sensor-to-sensor analysis in better perspective. For instance, these results suggested that habitat complexities with 5 and 4 classes are the more appropriate schemes to allow a meaningful comparison between the investigated sensors (Capolsini *et al.*, 2003). It is also depicted that the classification accuracies are not only controlled by the spectral and spatial resolutions but also by the internal configuration of the reef system. In which case, ASTER and ETM+ showed the poorer performance over the studied patch reef system.

After reaching the habitat scheme that overcomes the difficulties imposed by the reef system internal structures and that allowed a more meaningful comparison between sensors, AISA is still the more accurate sensor for this case study. Ikonos follows, with accuracies closely related to the ones achieved by ASTER when the latter undergoes bathymetric correction. Without bathymetric correction, ASTER performed poorer than ETM+.

Chapter 5

5. Conclusions

In general, remotely sensed data have proved to be useful for baseline reef habitat mapping. However, with recent trends of marine habitat degradation, it has become imperative to resolve the environment with a higher level of accuracy and detail. We compared a series of modern airborne and satellite sensors together with three different levels of image processing methods to help unveiling their relative capabilities and benefits for coral reef habitat mapping.

In this study several trends were noticed:

1. AISA data was highlighted to be significantly more accurate than the studied satellite sensors, by producing more accurate benthic habitat thematic maps including finer definition of geomorphological features.
2. Despite the spectral similarities with ETM+, Ikonos showed to be superior to it and to ASTER at every habitat complexity level. This demonstrates the benefits of the higher spatial resolution.
3. Over all the sensors, Ikonos is the one that exhibited more clearly a linear trend of improved accuracy with a decreased level of habitat complexity. At the coarser levels of habitats definition, 5 and 4 classes, Ikonos achieved P_o values greater than 80%. While at finer levels (>6 classes), it only reached moderate overall accuracies ($P_o < 70\%$).
4. AISA did not show major improvements in classification accuracy after bathymetric correction. It actually rendered high P_o over the studied coral reef environment without further image correction methods ($85\% > R_{rs} < 95\%$).

5. The Y_{ij} approach over Ikonos returned comparable results to those reached by the more basic R_{rs} image processing stage. Further, the R_B analytical model proved to be beneficial over the R_{rs} by improving the classification accuracy of Ikonos (>5%). Such small improvement, however, may not justify the use of costly high resolution lidar data for image bathymetric correction and shallow water coral reef habitat mapping. Other empirical or analytical methods to derive depth (H) for such purposes should be evaluated.
6. Bathymetric correction with R_B rendered significant improvements over ASTER (>30%). The improvement is such that overall classification accuracies compared to those for Ikonos at coarse levels of habitat complexities. ASTER proved to only be moderately appropriate for benthic habitat mapping over the studied patchy coral reef environment at a coarse habitat complexity level (4 and 5 classes) and after further image processing ($R_B > 80\%$).
7. Bathymetric correction using R_B was more beneficial for the broadband lower spatial resolution sensors (ASTER and ETM+) compared to the relative low gain in accuracy for AISA and Ikonos.
8. Overall, R_B performed better than Y_{ij} for all the sensors considered here.
9. The internal structure of the reef system controlled the proportion of classes comparable in this multi-sensor approach. Results showed that a meaningful scheme amenable for sensor-to-sensor comparison is only reached at a coarse habitat complexity level (5 and 4 classes). Here, the different densities of the “background” class *seagrass* modulated the classification results between habitat schemes with 10 to 6 classes. AISA and, in a smaller extent, Ikonos showed to be the sensors less influenced by the patchiness of the case study reef system. ETM+ only produced

moderate classification accuracies at the more basic level of habitat complexity (4 classes).

These findings support several trends that have been observed in previous studies (Turk and Caicos, Tahiti). However, this is the first multi-sensor comparison study that has been performed over an area as particular as the patch reef system in the Florida Keys, and that includes as part of its dataset lidar data for an objective bathymetric correction. Similarities on the results presented here with previous studies suggest that comparable trends can be generalized to different reef areas. Essentially, the selection of the more “appropriate” sensor still depends on particular objectives. However, multi-sensor studies accounting for various reef systems (*e.g.* biologically and morphologically different) will suggest what to expect when using a particular sensor for coral reef habitat mapping. Reports on costs and image-processing effectiveness together with analytical studies on the capabilities of modern sensors over different reef areas should point to the more suited sensor to remotely assess coral reefs.

As further work, it is suggested to update the cost-effectiveness assessment presented in Mumby *et al.* (1999b) by accounting for the more recent satellite sensors. QuickBird for example offer refined spatial resolution (2.44-meters multispectral and 0.61-meters panchromatic), being the only space sensor providing such level of footprint detail. QuickBird’s spectral bandwidths are similar to those of Ikonos and ETM+. Hyperion, in the other hand, offers same spatial resolution as ETM+ (30-meters). However, it is the first hyperspectral earth observing satellite sensor covering the whole spectral range within 220 spectral bands. It is expected that by accounting for the enhanced spatial and spectral capabilities of satellite sensors as such, it will be possible to narrow the gap between the degree of accuracy that can be derived from high resolution airborne and spaceborne sensors for coral reef assessment. It should elucidate as well the relative importance of the spatial and spectral resolutions in terms of thematic map accuracy. Further, such cost-effectiveness report should also include the time and effort effectiveness of using empirical or analytical image correction techniques, additionally to the image classification methods that will pay-off for the better map accuracies.

This study adds to the handful number of existing multi-sensor comparison studies targeting coral reef habitat mapping. Further evaluation on the capabilities of available remote sensors and different image processing techniques, will keep helping elucidating trends in the important task of accurate coral reef habitat inventorying, mapping and monitoring. Additionally, it also contribute clearing the path to the already raised discussion on the “necessity” for a spaceborne sensor with specifications better suited for underwater studies at various scales. Better suited spatial and spectral resolutions, together with an appropriate synoptic coverage for regional studies, should help to access and address more efficiently the different signs of worldwide coral reef degradation (Hochberg, Atkinson, and Andréfouët, 2003).

Appendix 1. Benthic sampling form used during the field campaign.

Survey Name: BNP Benthic Sampling Survey 2002					
BENTHIC SAMPLING FORM					
1. SITE DESCRIPTIONS					
		<input type="checkbox"/> ANNIVERSARY REEF AREA		<input type="checkbox"/> PACIFIC REEF AREA	
SITE #:	<input type="text"/>	DATE:	<input type="text"/> / <input type="text"/> / <input type="text"/>	TIME:	<input type="text"/> : <input type="text"/> : <input type="text"/>
			<small>DD MM YY</small>	DEPTH:	<input type="text"/> M
OBSERVER:	<input type="text"/>				
					<small>INITIALS</small>
LATITUDE:	<input type="text"/>	LONGITUDE:	<input type="text"/>	SLOPE:	<input type="text"/> °
				WATER VISIBILITY:	<input type="text"/> M
TRANSECT:	SECTION:	<input type="text"/>	BEARING:	<input type="text"/> °	LENGTH:
					<input type="text"/> M
			<small>WITH REF TO START XY</small>	PHOTOS:	<input type="text"/> <input type="text"/> <input type="text"/>
					<small>QTY FILM # SHOTS #/S</small>
2. PHYSICAL DESCRIPTIONS					
GENERAL DESCRIPTIONS					
<input type="text"/>	% COVERED SUBSTRATE	<input type="text"/>	% BARE SUBSTRATE	<input type="text"/>	% LIVE CORAL
<input type="text"/>		<input type="text"/>		<input type="text"/>	% SEAGRASS
COVERED SUBSTRATE					
SHAPE:	<input type="text"/>	1= MASSIVE	2= FLAT	3= HETEROGENEOUS	
SIZE:	<input type="text"/>	4= <50CM	5= 50 - 100CM	6= 1M - 2M	7= 2M - 5M
HEIGHT:	<input type="text"/>	10= <50CM	11= 50 - 100CM	12= 1M - 2M	13= >2M
BENHAB:	<input type="text"/>	14= LIVE CORAL	17= GORGONIAN	18= SPONGE	19= ZOANTHID
		21= ALGAE	<input type="text"/> A= TURF	B= CALCAREOUS	C= GREEN
				D= BROWN	E= CYANO
LIVE CORAL:					
SHAPE:	<input type="text"/>	1= MASSIVE	2= BRANCH	3= FOLIOSE	4= ENCRUST
SIZE:	<input type="text"/>	7= < 20CM	8= 20 - 50CM	9= 50 - 100CM	10= >100CM
HEIGHT:	<input type="text"/>	12= <20CM	13= 20 - 50CM	14= 50 - 100CM	15= >100CM
GENUS:	<input type="text"/>	17= ACROPORA	18= PORITES	19= AGARICIA	20= MONTASTRABA
				21= SIDERASTREA	22= DIP LORIA
		23= OTHER:		SPECIE:	
BARE SUBSTRATE					
SEDIMENTS:	<input type="text"/>	1= SAND	2= RUBBLE	3= MIXED	4= OTHER:
					SIZE: <input type="text"/> CM
SEAGRASS					
COVER:	<input type="text"/>	1= 0 - 25%	2= 25 - 50%	3= 50 - 75%	4= 75 - 100%
TEXTURE:	<input type="text"/>	4= PATCHY	5= CONTINUOUS	6= NETWORK	
SPECIE:	<input type="text"/>	7= THALASIA	8= SYRINGODIUM	9= HALIMEDA	10= OTHER:
COMMENTS:					
.....					
.....					
.....					
DTP					

Appendix 2. Producer and user accuracies as derived from error matrices for AISA and Ikonos image classification at every habitat complexity and image processing level.

	AISA						Ikonos					
	Rrs		RB		Yij		Rrs		RB		Yij	
	Producer	User	Producer	User								
Four classes												
Live covered substrate	96.9	91.2	93.8	96.8	93.8	100.0	82.4	43.8	82.4	53.9	82.4	43.8
Seagrass	93.5	98.6	98.7	97.4	98.7	97.4	82.0	97.1	90.1	96.7	82.0	97.1
Algal dominated	80.0	100.0	100.0	100.0	100.0	100.0	100.0	8.3	100.0	10.0	100.0	8.3
Carbonate sand	100.0	62.5	100.0	100.0	100.0	83.3	87.5	93.3	56.3	100.0	87.5	93.3
Five classes												
Dense live covered substrate	95.5	95.5	90.9	95.2	100.0	100.0	71.4	23.8	73.3	47.8	66.7	37.0
Sparse live covered substrate	60.0	100.0	70.0	100.0	70.0	100.0	100.0	54.6	100.0	62.5	100.0	71.4
Seagrass	97.4	94.9	100.0	95.1	98.7	96.2	80.6	99.3	87.3	97.2	81.7	94.9
Algal dominated	80.0	100.0	100.0	100.0	100.0	100.0	100.0	6.7	0.0	0.0	0.0	0.0
Carbonate sand	100.0	62.5	100.0	100.0	100.0	83.3	87.5	100.0	62.5	90.9	81.3	86.7
Six classes												
Dense live covered substrate	95.5	95.5	95.5	95.5	100.0	95.7	58.3	46.7	83.3	55.6	75.0	45.0
Sparse live covered substrate	70.0	100.0	80.0	100.0	80.0	88.9	80.0	30.8	80.0	30.8	80.0	26.7
Dense seagrass	100.0	90.6	100.0	93.6	96.6	96.6	75.2	81.0	77.0	87.0	71.7	86.2
Medium-sparse seagrass	97.9	100.0	97.9	100.0	97.9	100.0	47.8	61.1	63.0	65.9	47.8	55.0
Algal dominated	80.0	100.0	100.0	100.0	100.0	100.0	0.0	0.0	0.0	0.0	0.0	0.0
Carbonate sand	100.0	71.4	100.0	83.3	100.0	83.3	82.4	93.3	58.8	100.0	82.4	93.3
Seven classes												
Dense live covered substrate	95.5	95.5	95.5	95.5	95.5	100.0	35.7	33.3	62.5	50.0	25.0	40.0
Sparse live covered substrate	80.0	100.0	80.0	100.0	80.0	100.0	100.0	66.7	85.7	60.0	85.7	54.6
Dense seagrass	100.0	92.9	100.0	100.0	100.0	92.9	81.3	85.7	85.4	81.7	83.2	84.1
Medium-sparse seagrass	97.9	97.9	97.9	95.9	97.9	100.0	50.0	57.9	50.9	81.1	42.4	69.4
Seagrass with distinct coral patches	87.5	87.5	87.5	87.5	93.8	83.3	62.5	62.5	85.7	48.0	85.7	44.4
Algal dominated	80.0	100.0	100.0	100.0	100.0	100.0	100.0	6.7	100.0	25.0	100.0	18.2
Carbonate sand	100.0	71.4	100.0	83.3	100.0	83.3	58.8	100.0	75.0	100.0	87.5	82.4
Eight classes												
Dense live covered substrate	95.5	95.5	95.5	95.5	95.5	100.0	28.6	57.1	37.5	27.3	35.7	62.5
Sparse live covered substrate	80.0	100.0	80.0	100.0	80.0	100.0	50.0	50.0	85.7	60.0	50.0	42.9
Dense seagrass	100.0	92.9	100.0	92.9	100.0	92.9	78.0	81.6	72.5	80.5	75.8	83.1
Medium-sparse seagrass	52.4	91.7	52.4	84.6	47.6	90.9	85.7	46.2	57.1	50.0	85.7	50.0
Medium density seagrass	96.3	70.3	92.6	69.4	96.3	68.4	31.0	44.8	50.0	63.9	35.7	41.7
Seagrass with distinct coral patches	87.5	87.5	87.5	87.5	87.5	82.4	66.7	57.1	50.0	32.1	66.7	57.1
Algal dominated	80.0	100.0	100.0	100.0	100.0	100.0	100.0	5.9	0.0	0.0	100.0	6.7
Carbonate sand	100.0	83.3	100.0	100.0	100.0	100.0	75.0	80.0	73.3	84.6	68.8	84.6
Nine classes												
Dense live covered substrate	95.5	95.5	95.5	95.5	95.5	100.0	42.9	37.5	62.5	45.5	62.5	45.5
Sparse live covered substrate	80.0	100.0	80.0	88.9	80.0	80.0	66.7	57.1	87.5	70.0	50.0	57.1
Dense seagrass	100.0	92.9	100.0	92.9	100.0	92.9	69.9	85.5	77.5	82.1	76.4	87.2
Medium density seagrass	66.7	87.5	100.0	100.0	66.7	93.3	50.0	40.0	66.7	60.0	66.7	66.7
Sparse seagrass	75.0	66.7	62.5	71.4	87.5	87.5	50.0	25.0	100.0	75.0	100.0	75.0
Medium density seagrass	100.0	79.2	100.0	90.5	94.7	85.7	46.0	41.5	51.2	59.5	51.2	53.7
Seagrass with distinct coral patches	87.5	73.7	87.5	73.7	93.8	68.2	50.0	52.9	50.0	52.6	65.0	61.9
Algal dominated	80.0	100.0	100.0	100.0	100.0	100.0	100.0	9.1	100.0	22.2	100.0	25.0
Carbonate sand	60.0	100.0	100.0	100.0	60.0	100.0	60.0	75.0	69.2	81.8	92.3	75.0
Ten classes												
Dense live covered substrate	86.4	95.0	86.4	95.0	86.4	90.5	33.3	28.6	42.9	25.0	14.3	11.1
Dense live covered reef edge	91.3	87.5	91.3	91.3	78.3	90.0	45.5	27.8	22.2	9.1	22.2	6.3
Sparse live covered substrate	80.0	100.0	62.5	71.4	80.0	80.0	27.3	33.3	87.5	63.6	87.5	63.6
Dense seagrass	100.0	92.9	100.0	86.7	100.0	76.5	73.4	72.3	67.9	84.6	71.6	82.9
Medium density seagrass on sandy bottom	66.7	87.5	66.7	82.4	66.7	93.3	55.6	83.3	55.6	62.5	55.6	62.5
Sparse seagrass	75.0	66.7	62.5	71.4	87.5	87.5	50.0	33.3	33.3	25.0	33.3	50.0
Medium density seagrass on sandy bottom with algae and rubble	100.0	79.2	100.0	90.5	94.7	85.7	13.6	35.3	46.5	58.8	34.9	79.0
Seagrass with distinct coral patches	87.5	70.0	87.5	70.0	93.8	68.2	72.2	52.0	57.9	57.9	68.4	59.1
Algal dominated	80.0	100.0	100.0	100.0	100.0	100.0	0.0	0.0	50.0	10.0	50.0	12.5
Carbonate sand	60.0	100.0	100.0	100.0	60.0	100.0	73.3	84.6	61.5	88.9	84.6	84.6

Reviewed Literature

- Andréfouët S, Hochberg EJ, Payri C, Atkinson MJ, Muller-Karger FE, Ripley H (2003a) Multi-scale remote sensing of microbial mats in an atoll environment. *International Journal of Remote Sensing* 24: 2661-2682.
- Andréfouët S, Robinson JA, Hu C, Feldman G, Salvat B, Payri C, Muller-Karger FE (2003b) Influence of the spatial resolution of SeaWiFS, Landsat 7, SPOT and International Space Station data on determination of landscape parameters of Pacific Ocean atolls. *Canadian Journal of Remote Sensing* 29(2): 210-218.
- Andréfouët S, Kramer PA, Torres-Pulliza D, Joyce K, Hochberg E, Garza-Pérez R, Mumby P, Riegl B, Yamano H, White W, Zubia M, Brock J, Phinn S, Naseer A, Hatcher B, Muller-Karger F (2003c) Multi-site evaluation of IKONOS data for classification of tropical coral reef environments. *Remote Sensing of Environment* 88: 128-143.
- Andréfouët S, Mumby PJ, McField M, Hu C, Muller-Karger FE (2002a) Revisiting coral reef connectivity. *Coral Reefs Special Issue Large Scale Dynamics of Coral Reef Systems*, 21:43-48.
- Andréfouët S, Berkelmans R, Odriozola L, Done TJ, Oliver JK, Muller-Karger FE (2002b) Choosing the appropriate spatial resolution for monitoring coral bleaching events using remote sensing. *Coral Reefs*, 21: 147-154.
- Andréfouët S, Claereboudt M, Matsakis P, Pages J, Dufour P (2001) Typology of atoll rims in Tuamotu Archipelago (French Polynesia) at landscape scale using SPOT HRV images. *International Journal of Remote Sensing* 22: 987-1004.
- Andréfouët S, Claereboudt M (2000) Objective class definitions using correlation of similarities between remotely sensed and environmental data. *International Journal of Remote Sensing*, 21:1925-1930.
- Atkinson PM, Curran PJ (1997) Choosing an Appropriate Spatial Resolution for Remote Sensing Investigations. *Photogrammetric Engineering and Remote Sensing*, 63(12): 1345-1351.
- Armstrong, RA (1993) Remote Sensing of submerged vegetation canopies for biomass estimation. *International Journal of Remote Sensing*, 14: 10-16.
- Bellwood D, Hughes T (2001) Regional-scale assembly rules and biodiversity of coral reefs. *Science*, 292: 1532 –1534.
- Bierwirth PN, Lee TJ, Burne RV (1993) Shallow sea-floor reflectance and water depth derived by unmixing multispectral imagery. *Photogrammetric Engineering and Remote Sensing*, 59: 331-338.
- Brock JC, Wright CW, Clayton TD, Nayegandhi A (2004) Optical rugosity analysis of coral reef status in Biscayne National Park, Florida. *Coral Reefs*, 23: 48-59.

- Benson BJ, MacKenszie MD (1995) Effects of sensor spatial resolution on landscape structure parameters. *Landscape Ecology*, 10(2): 113-120.
- Bray JR, Curtis JT (1957) An ordination of the upland forest communities of Southern Wisconsin. *Ecology Monograph*, 27: 325-349.
- Capolsini P, Andréfouët S, Rion C, Payri C (2003) A comparison of Landsat ETM+, SPOT HRV, Ikonos, ASTER, and airborne MASTER data for coral reef habitat mapping in South Pacific islands. *Canadian Journal of Remote Sensing*, 29: 187-200.
- Clarke KR, Warwick RM (1994) Change in marine communities: an approach to statistical analysis and interpretation. *Natural Environment Research Council*, Plymouth
- Congalton RG (1991) A review of assessing the accuracy of classifications of remotely sensed data. *Remote Sensing of the Environment*, 37: 35-46.
- Cullinan VI, Thomas JM (1992) A comparison of quantitative methods for examining landscape pattern and scale. *Landscape Ecology*, 7(3): 211-227.
- Fraser RS, Mattoo S, Yeh E, and McClain C (1997) Algorithm for atmospheric and glint corrections of satellite measurements of ocean pigment. *Journal of Geophysical Research*, 102(17): 107-118.
- Glynn PW (1996) Coral reef bleaching: facts, hypotheses and implications. *Global Change Biology*, 2: 495-509.
- Gordon HR (1992) Radiative transfer in the atmosphere for correction of ocean color remote sensors. *Ocean Colour: Theory and Applications in a Decade of CZCS Experience*, V Barale and PM Schlittenhardt Eds., Kluwer Academic, Dordrecht, 33-77.
- Green EP, Mumby PJ, Edwards AJ, Clark CD (1996) A review of remote sensing for the assessment and management of tropical coastal resources. *Coastal Management*, 24:1-40.
- Gregg WW, Carder KL (1990) A simple spectral solar irradiance model for cloudless maritime atmospheres. *Limnology and Oceanography*, 35: 1657-1675.
- Hedley JD, Mumby PJ (2002) Biological and remote sensing perspectives of pigmentation in coral reef organisms. *Advances in Marine Biology*, 43: 277-317.
- Hochberg EJ, Atkinson MJ (2003a) Capabilities of remote sensors to classify coral, algae, and sand as pure and mixed spectra. *Remote Sensing of Environment*, 85: 174-189.
- Hochberg EJ, Andréfouët S, Tyler MR (2003b) Sea surface correction of high spatial resolution Ikonos images to improve bottom mapping in near-shore environments. *IEEE Transactions on Geoscience and Remote Sensing*, 41: 1724-1729.

- Hochberg EJ, Atkinson MJ, Andréfouët S (2003c) Spectral reflectance of coral reef bottom-types worldwide and implications for coral reef remote sensing. *Remote Sensing of Environment*, 85: 159-173.
- Hu C, Carder K (2002) Atmospheric-correction for airborne sensors: comments on a scheme used for CASI. *Remote Sensing of Environment*, 79: 134-137.
- Jaap WC (1984) The ecology of the south Florida coral reefs: a community profile. *Report no. FWS/BS-82/08, US Fish and Wild Life Service, Office of Biological Services*, Washington DC 138p.
- Jaap WC, Porter JW, Wheaton J, Hackett K, Lybolt M, Callahan MK, Tsokos C, Yanev G (2001) Environmental Protection Agency/Florida Keys National Marine Sanctuary Coral Reef Monitoring Project: Updated executive summary 1996-2000. Washington DC: EPA. 22p.
- James W. Porter, Sarah K. Lewis, and Karen G. Porter (1999) The effect of multiple stressors on the Florida Keys coral reef ecosystem: A landscape hypothesis and a physiological test. *Limnology and Oceanography*, 44: 941-949.
- Kleypas JA, Buddemeier RW, Gattuso J-P (2001). The future of coral reefs in an age of global change. *International Journal of Earth Sciences*, 90: 426-437.
- Lee ZP, Carder KL, Hawes SK, Steward RG, Peacock TG, Davis CO (1994) A model for interpretation of hyperspectral remote sensing reflectance. *Applied Optics*, 33: 5721-5732.
- Lee ZP, Carder KL, Mobley CD, Steward RG and Patch JS (1999) Hyperspectral remote sensing for shallow waters: 2. Deriving bottom depths and water properties by optimization. *Applied Optics*, 38: 3831-3843.
- Lyzenga DR (1981) Remote sensing of bottom reflectance and water attenuation parameters in shallow water using aircraft and Landsat data. *International Journal of Remote Sensing*, 2:71-82.
- Lyzenga DR (1978) Passive remote sensing techniques for mapping water depth and bottom features. *Applied Optics*, 17: 379-383.
- Ma Z, Redmond RL (1995) Tau coefficient for accuracy assessment of classification of remote sensing data. *Photogrammetric Engineering and Remote Sensing*, 61: 435-439.
- Maritorena S, Morel A, Gentili B (1994). Diffuse reflectance of oceanic shallow waters: influence of water depth and bottom albedo. *Limnology and Oceanography*, 39: 1689-1703.
- Maritorena S (1996) Remote sensing of the water attenuation in coral reefs: a case study in French Polynesia. *International Journal of Remote Sensing*, 17: 155-166.
- Marszalek DS, Babashoff G, Noel MR, Worley DR (1997) Reef distribution in South Florida. *Proceedings of the 3rd International Coral Reef Symposium*, Miami 2: 233-229.

- Moberg F, Folke C (1999) Ecological goods and services of coral reef ecosystems. *Ecological Economics*, 29: 215-233.
- Mobley CD (1999) Estimation of the remote-sensing reflectance from above-water surface measurements. *Applied Optics* 38: 7442-7455.
- Mobley CD (1995) Hydrolight 3.0 User's Guide. *SRI Project 5632*.
- Mobley CD (1994) Light and water: radiative transfer in natural waters. 592p. San Diego, California: Academic Press.
- Mobley CD, Gentili B, Gordon HR, Jin Z, Kattawar GW, Morel A, Reinersman P, Stamnes K, Stavn RH (1993). Comparison of numerical models for computing underwater light fields. *Applied Optics* 32: 7484-7504.
- Morel A, Maritorena S (2001) Bio-optical properties of oceanic waters: A reappraisal. *Journal of Geophysical Research*, 106: 7163-7180.
- Mumby PJ, Skirving W, Strong AE, Hardy JT, LeDrew EF, Hochberg EJ, Stumpf RP, David LT (2004). Remote sensing of coral reefs and their physical environment. *Marine Pollution Bulletin*, 48: 219-228.
- Mumby PJ, Edwards AJ (2002). Mapping marine environments with IKONOS imagery: enhanced spatial resolution can deliver greater thematic accuracy. *Remote Sensing of Environment*, 82: 248-257.
- Mumby PJ (2001). Beta and habitat diversity in marine systems: a new approach to measurement, scaling and interpretation. *Oecologia*, 128: 274-280.
- Mumby PJ, Harborne AR (1999a) Development of a systematic classification scheme of marine habitats to facilitate regional management and mapping of Caribbean coral reefs. *Biological Conservation*, 88: 155-163.
- Mumby PJ, Green EP, Edwards AJ, Clark CD (1999b). The cost-effectiveness of remote sensing for tropical coastal resources assessment and management. *Journal of Environmental Management*, 55: 157-166.
- Mumby PJ, Clark CD, Green EP, Edwards AJ (1998a) Benefits of water column correction and contextual editing for mapping coral reefs. *International Journal of Remote Sensing*, 19(1): 203-210.
- Mumby PJ, Green EP, Clark CD, Edwards AJ (1998b) Digital analysis of multispectral airborne imagery of coral reefs. *Coral Reefs* 17: 59-69.
- Palandro D, Andréfouët S, Dustan P, Muller-Karger FE (2003) Change detection in coral reef communities using the IKONOS sensor and historic aerial photographs. *International Journal of Remote Sensing*, 24: 873-878.

- Philpot WD (1989) Bathymetric mapping with passive multispectral imagery. *Applied Optics*, 28: 1569-1578.
- Phinn S (1998) A framework for selecting appropriate remotely sensed data dimension for environmental monitoring and management. *International Journal of Remote Sensing*, 19: 3457-3463.
- Porter JW and Meier OW (1992) Quantification of loss and change in Floridian reef coral populations. *American Zoologist* 32:625-640.
- Purkis SJ, Pasterkamp R (2004) Integrating in situ reef-top reflectance spectral with Landsat TM imagery to aid shallow-tropical benthic habitat mapping. *Coral Reefs*, 23: 5-20.
- Richards JA (1999) Remote sensing digital image analysis. *Springer-Verlag*, Berlin p 240.
- Shinn EA, Lidz BH, Kindinger JL, Hudson JH, Halley RB (1989) A guide to the modern carbonate environments of the Florida Keys and the Dry Tortugas. 28th *International Geological Congress*, Washington DC.
- Smith RC, and Baker KS (1981) Optical properties of the clearest natural waters (200-800 nm). *Applied Optics*, 20: 177-184.
- Stehman SV (1997) Selecting and interpreting measures of thematic classification accuracy. *Remote Sensing of Environment*, 62: 77-89.
- Stumpf RP, Holderied K, Sinclair M (2003) Determination of water depth with high-resolution satellite imagery over variable bottom depths. *Limnology and Oceanography*, 48: 547-556.
- Toole DA, Siegel DA, Menzies DW, Neumann MJ, Smith RC (2000) Remote-sensing reflectance determinations in the coastal ocean environment: impact of instrumental characteristics and environmental variability. *Applied Optics*, 39: 456-469.
- US Global Change Research Program (2003) Our Changing Planet: The FY 2003 Global Change Research Program: A Report by the Subcommittee on Global Change Research, Washington, DC: National Science and Technology Council.
- Vermote EF, Tanre D, Deuze JL, Herman M, Morcrette JJ (1997) Second simulation of the satellite signal in the solar spectrum, 6S: an overview. *IEEE Transaction of Geosciences and Remote Sensing*, 35: 675-686.
- Wilkinson C (Ed.) (2002) Status of coral reefs of the world; 2002. Townsville, Queensland, Australia: Australian Institute of Marine Science, 363 pp.
- Wright CW, Brock J (2002) EAARL: A lidar for mapping shallow coral reefs and other coastal environments, 7th *International Conference on Remote Sensing for Marine and Coastal Environments: Miami, FL*.